UC Riverside

UC Riverside Electronic Theses and Dissertations

Title

Engineering Graphene Quantum Dots: Synthesis and Application for Lithium-Ion Photo-Rechargeable Battery

Permalink

https://escholarship.org/uc/item/3th3n81w

Author

Kim, Jiyong

Publication Date

2022

Peer reviewed|Thesis/dissertation

eScholarship.org Powered by the California Digital Library
University of California

UNIVERSITY OF CALIFORNIA
RIVERSIDE

Engineering Graphene Quantum Dots: Synthesis and Application for Lithium-Ion Photo-Rechargeable Battery

A Dissertation submitted in partial satisfaction
of the requirements for the degree of

Doctor of Philosophy

in

Chemical and Environmental Engineering

by

Jiyong Kim

June 2022

Dissertation Committee:
  Dr. Alfredo A. Martinez-Morales, Chairperson
  Dr. Juchen Guo
  Dr. Boniface Fokwa

Copyright by
Jiyong Kim
2022

The Dissertation of Jiyong Kim is approved:

____

____

____
Committee Chairperson

University of California, Riverside

Acknowledgement

I would like to express my deep sense of gratitude to my advisor Dr. Alfredo A. Martinez-Morales, for his continuous support and encouragement throughout my Ph.D. study. With his support, I was able to complete this dissertation. In addition, I am also deeply indebted to my committee members, Dr. Juchen Guo and Dr. Boniface P.T. Fokwa, for their time and effort in reviewing this work.

I would like to gratefully acknowledge my lab mate, Dr. Taehoon Lim, Dr. Fei Gu, Dr. Seungjin Lee, Dr. Minerva Uribe-Robles, for their support and crucial contribution, which made them a backbone of this research and so to the thesis. Their involvement with their originality has triggered and nourished my intellectual maturity.

It is my pleasure to express my gratitude wholeheartedly to my family. My parents deserve special mention for their inseparable support and prayers. My father, Jung-Gyu Kim, is the person who put the fundament of my learning character, showing me the joy of intellectual pursuit ever since I was a child. My mother, Kyung-Sook Kim, is the one who sincerely raised me with her caring and gentle love. And I would like to express my gratitude for my sisters. Finally, I would like to dedicate my work to Tofu and my loving wife, Ari Min.

ABSTRACT OF THE DISSERTATION

Engineering Graphene Quantum Dots: Synthesis and Application for Lithium-Ion Photo-Rechargeable Battery

by

Jiyong Kim

Doctor of Philosophy, Graduate Program in Chemical and Environmental Engineering
University of California, Riverside, June 2022
Dr. Alfredo A. Martinez-Morales, Chairperson

Fossil fuels have been used as the primary source of energy to meet the growing demand for electric energy consumption. The use of fossil fuels results in carbon dioxide and greenhouse gas emissions, contributing to the acceleration of climate change and global warming. Therefore, more energy should be produced from renewable energy resources to lessen the energy reliance on fossil fuels. In particular, solar energy is regarded as the most promising renewable energy resource or alternative to fossil fuels because it is not only unlimited but also pollution-free. However, the main concern of solar energy is highly dependent on weather and environmental conditions, as well as the high initial facility cost. The intermittency of solar photovoltaic (PV) system can be alleviated by the use of battery. In addition, the capacity limitations of battery can also be overcome with PV system. The traditional PV-battery system allows significant energy losses to occur due to connections between individual components, affecting the efficiency of overall system. The direct integration of PV-battery system has a potential to minimize the energy losses and to reduce the facility costs by simplifying the device architecture.

The main objectives of this dissertation are focused on 1) the development of a simple and cost-effective photo-rechargeable battery system combining solar cells with batteries into a single device, 2) selective synthesis of oxidized graphene quantum dots from graphite rod as photosensitizers, and 3) the performance improvement of the photo-rechargeable battery using graphene quantum dots (GQDs) and ruthenium-based dye (N719). Chapter 2 focuses on understanding the structure and operation mechanism of photo-rechargeable battery, consisting of a TiO_2 photoanode, a $LiFePO_4$ cathode, and LiTFSI in PC electrolyte. The performance and stability tests of photo-rechargeable battery is examined by electrochemical measurements. Chapter 3 describes the synthesis of GQDs that exhibit a variety of excellent properties including high carrier transport mobility, large surface area, tunable bandgaps, quantum confinement, and environmental friendliness. The oxidized GQDs are selectively synthesized by the electrochemical exfoliation method and toluene post-treatment. The chemical, structural, and optical properties of synthesized GQDs are evaluated for the use of photo-rechargeable battery. Chapter 4 discusses how GQDs work and affect the performance of photo-rechargeable battery. In addition, the fabrication process of photo-rechargeable batteries which utilize the TiO_2, GQDs/TiO_2, N719/TiO_2, N719/GQDs/TiO_2 as the photoelectrodes are discussed. The performance and characteristic tests of four different photoanode

implemented in the photo-rechargeable batteries is investigated. In conclusion, the photo-rechargeable battery with N719/GQDs/TiO_2, shows significantly improved conversion efficiency and cyclic performance under illumination compared to the photo-rechargeable battery with pristine TiO_2. GQDs have a crucial role in reducing the internal resistance, transferring electrons between TiO_2 and N719, and absorbing more dye. The conclusions and remarks of the dissertation are summarized in Chapter 5.

Table of Contents

Chapter 3. Selective Synthesis of Oxidized Graphene Quantum Dots 43

Chapter 4. Engineering Graphene Quantum Dots: Application for Photo-rechargeable Battery 66

List of Figures

List of Tables

Chapter 1. Introduction

1.1 Renewable Energy

The overall energy consumption in the world has continuously increased due to the rapid growth of population and industrial development since the first industrial revolution in the middle of 18th century. Figure 1.1 indicates the higher expectations of global energy use from 2020 to 2050 due to the increase in electricity demand.[1] The major sources of energy production come in many different forms such as nuclear energy, fossil fuels, and renewable energy.[2] Especially, fossil fuels including coal, natural gas, and petroleum have been used as primary sources of energy.[3] The combustion of fossil fuels releases carbon dioxide (CO_2) and greenhouse gases, accelerating the global warming and climate change.[4] Therefore, the policies and guidance of government for energy production should be directed toward increasing the proportion of renewable energy to reduce the dependance of fossil fuels.[5]

Renewable energy is energy from natural sources including sunlight, wind, geothermal heat, biomass, and tides.[6] Renewable energy has many advantages such as sustainability, reliability of supplying energy, environmentally friendliness, less operating and maintenance cost, and the increase in job openings and country's energy dependance.[7] In Figure 1.1, the global energy usage is predicted to increase around 50% from 2020 to 2050. Both natural gas and petroleum productions are expected to rise slightly through 2050 with growing energy demand. Energy production from nuclear and coal have remained almost unchanged since 2010. On the other hand, it is anticipated that

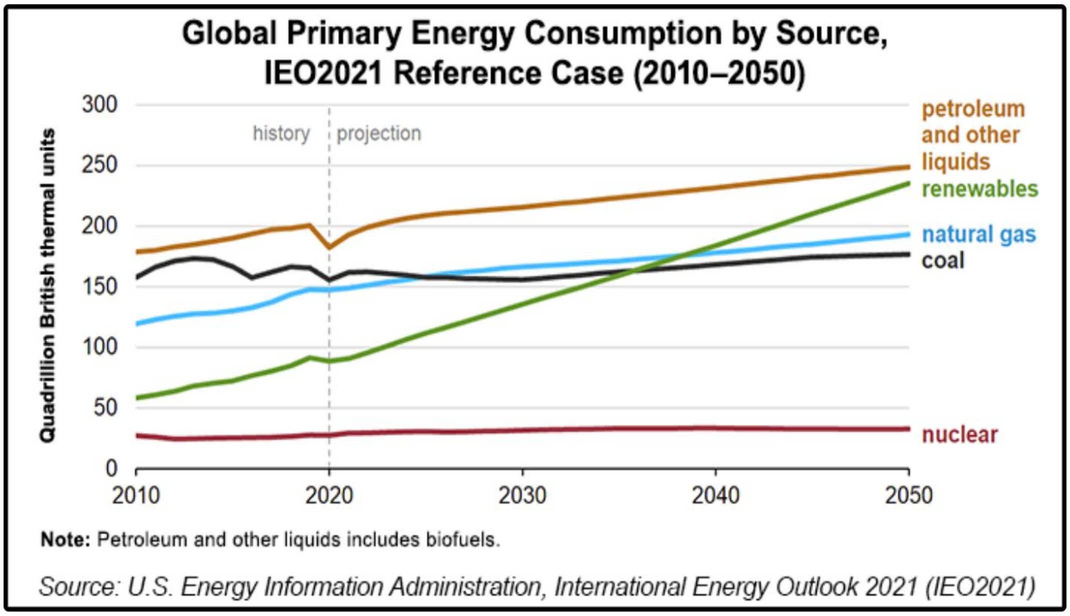

Figure 1.1 Perspective global energy consumption by energy source.[1]

renewable energy production has consistently increased by 400% from 2010 to 2050. Energy production from renewable sources has been spotlighted continuously. All sources of renewable energy have mostly been used for electricity generation. Furthermore, geothermal steam, biomass, and solar sources are used directly for heating. Especially, biofuels (ethanol and biodiesel) obtained from biomass are also used for transportation.[8]

Global electricity generation is increasingly produced by renewable energy sources. Figure 1.2 represents the anticipated electricity production by renewable source from 2010 to 2050.[9] Unlike other renewable energy sources, most of rise in renewable electricity production is contributed by wind and solar energy, which account for 50% of electricity generation in 2018. In addition, The proportion of wind and solar energy approaches to around 73% in 2050. However, growth in wind energy production is expected to be settled due to the noise pollution, expensive installation cost, and limited installation space. Especially, wind turbines require large amount of wind and also produce noise from the revolving rotor blades. Therefore, wind turbines cannot find easily near the residential area. The limited space for installation lead to the low density of wind energy production.[10] On the contrary, solar energy is the sharply growing energy among the renewable energy for electricity generation. In 2020, solar panels reached 760 GW of total global capacity, corresponding to the almost 3 percent of electricity in the world.[11] In addition, From 2010 to 2020, the cost of residential, commercial-rooftop, and utility-scale PV systems has reduced by around 64%, 69%, and 82%, respectively. As a result, total 85% cost of solar modules including hardware and inverter has been declined

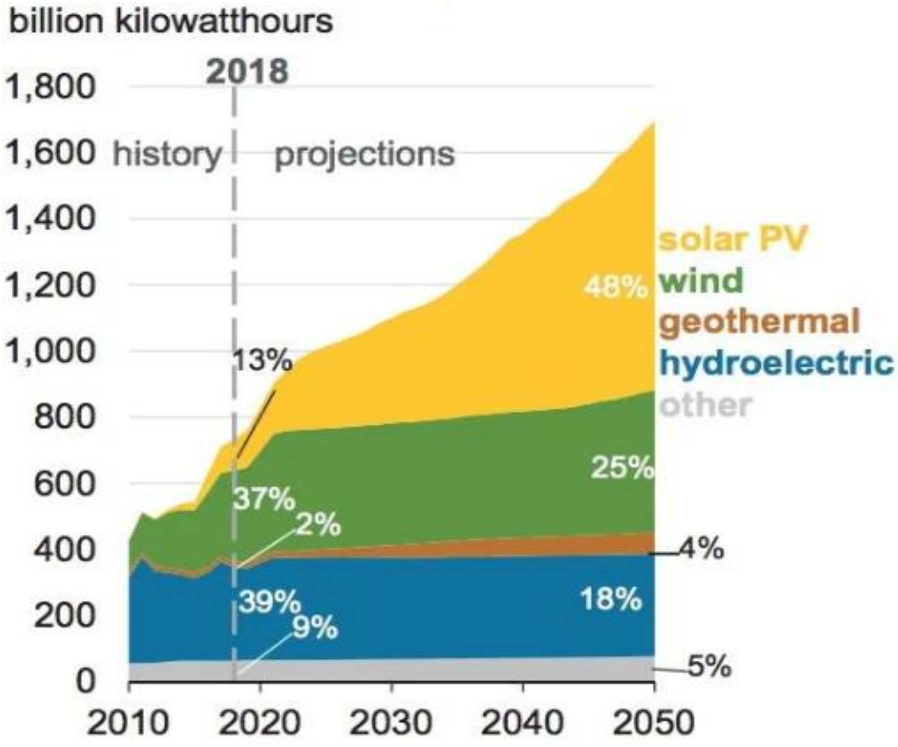

Figure 1.2 Renewable electricity generation by source, in billion kWh.[10]

for a decade.[12] Therefore, the research and development of solar photovoltaic technologies are indispensable for increasing portion of renewable energy. Silicon photovoltaic cell are widely used for electricity production due to the high and stable cell efficiencies (25%).[13] However, silicon panels also have difficulties in applying to other devices because they are heavy and have a high manufacturing cost and space restriction for installation.

1.2 Photo-rechargeable Batteries

The main issue of solar energy is highly dependent on weather and environmental conditions, resulting in energy fluctuations. Therefore, the solar photovoltaic (PV) system should be combined with batteries to relieve the intermittency of solar energy because the electric energy can be stored during the day and released during nighttime. In addition, the capacity limitations of batteries can be overcome with solar PV systems.[14, 15] Thus, the integration of PV systems and batteries provide a significant effect on the practicality of renewable energy devices by compensating their defects.

The traditional PV-battery system is composed of solar PV system and energy storage system as two individual units and connected with external electrical wires as shown in Figure 1.3.(a).[15, 16] Such PV-battery system is heavy, bulky, expensive, inflexible, and complicated. In addition, the electrical wires and connections between each component result in significant energy losses, affecting the efficiency of overall PV-battery system.[17] On the contrary, the integrated PV-battery systems as shown in figure 1.3.(b) are compact, lightweight, and energy efficient by minimizing the overall volume

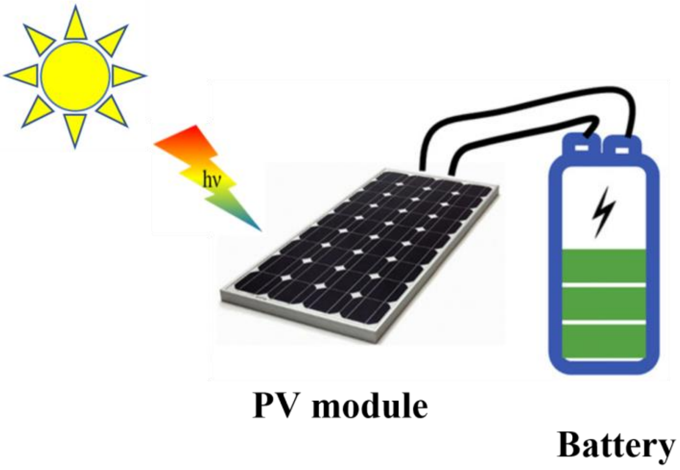

(a) Traditional PV-battery system

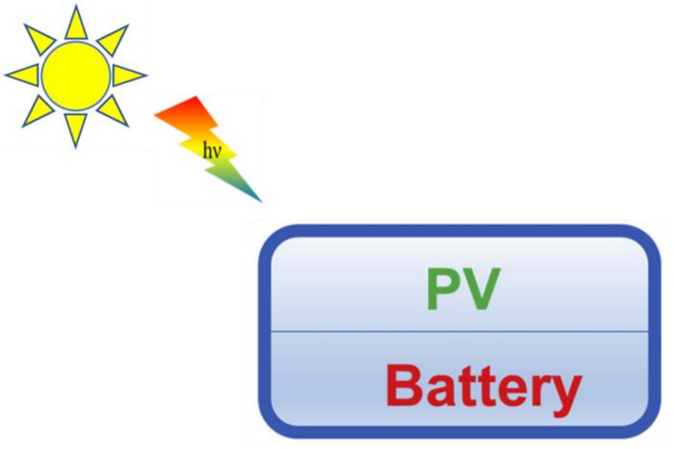

(b) Integrated PV-battery system

Figure 1.3 A schematic diagram of (a) Traditional and (b) Integrated PV-battery systems.[15]

of the PV-battery systems. Moreover, the structure of integrated PV-battery systems reduces the production cost because they require less wiring and packaging. However, the integrated PV-battery systems have a lot of challenges such as low stability and efficiency. Such challenges should be resolved to increase the practicality and to commercialize this technology.

Figure 1.4 shows the four different configuration of PV-battery systems.[15] The integrated PV-battery system can be categorized into two major systems. Figure 1.4.(a) indicates the traditional (or conventional) PV-battery system is composed of two independent units including PV and battery systems. Figure 1.4 (b-d) represent the circuit diagram of integrated PV-battery system. The integrated PV-battery systems are classified by the number of electrodes. In three electrode systems (Figure 1.4.(b) and 1.4.(c)), one of the electrodes is used as cathode or anode at the middle of PV-battery device. In two electrode system (Figure 1.4.(d)), one of the electrodes also play a role in photoelectrode, converting light energy to electric energy.

1.3 Solar Cell Fundamentals

A solar cell, also called photovoltaic (PV) cell, converts the light energy into the electric energy through the photovoltaic effect.[18] Semiconductors are mainly used as electrodes in photoelectrochemistry due to their light absorbance.[19] The electronic and optical properties of solid-state materials are explained on the basis of band theory.[20] Unlike metals (or conductors), the semiconductors have a bandgap between the valence and conduction bands. Furthermore, the type of solar cell can be largely categorized by

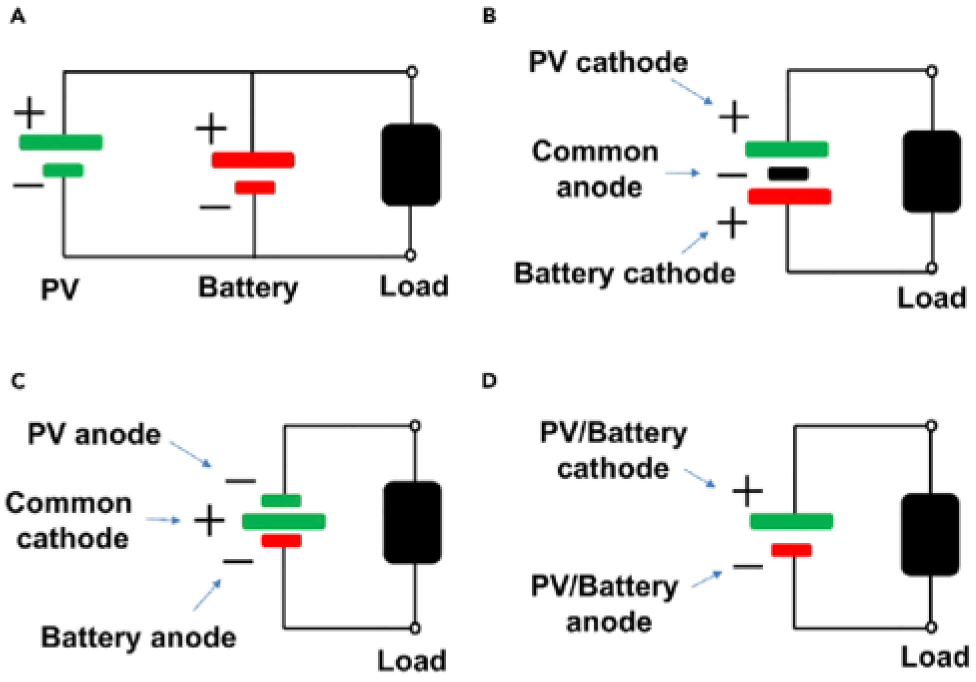

Figure 1.4 Circuit diagram of various types of PV-battery systems.[15]

the material (organic and inorganic).

1.3.1 Semiconductor Theory

The materials are classified as conductor, semi-conductor, and insulator, depending on the bandgap as shown in Figure 1.5.[21, 22] The band diagram depicts conduction band, valence band, bandgap, and fermi level. The conduction band is the lowest range of vacant electronic states without free electrons, while the valence band is the highest range of electronic states filled with free electrons. The electrons jump up into from the valence band to conduction band by electron excitation. The fermi level is the energy state that hypothesized 50% chance of being occupied electrons.[23] In addition, the electronic property of materials is determined by the position of fermi level of semiconductor. The bandgap is the energy difference between valence band and conduction band. The bandgap requires the minimum energy to jump up from valence band to conduction band.[24] Conductors (metals) have no bandgap because the conduction band and valence band are overlapped. Therefore, electrons can easily move between both bands. On the contrary, insulators have a large bandgap that required a lot of energy to move electrons from valence band to conduction band meaning the material is non-conductive. Semiconductors have a smaller bandgap compared to insulators. In semiconductors, the electrons can freely jump out of the band once the energy of photon is higher than band gap ($hv > E_g$).

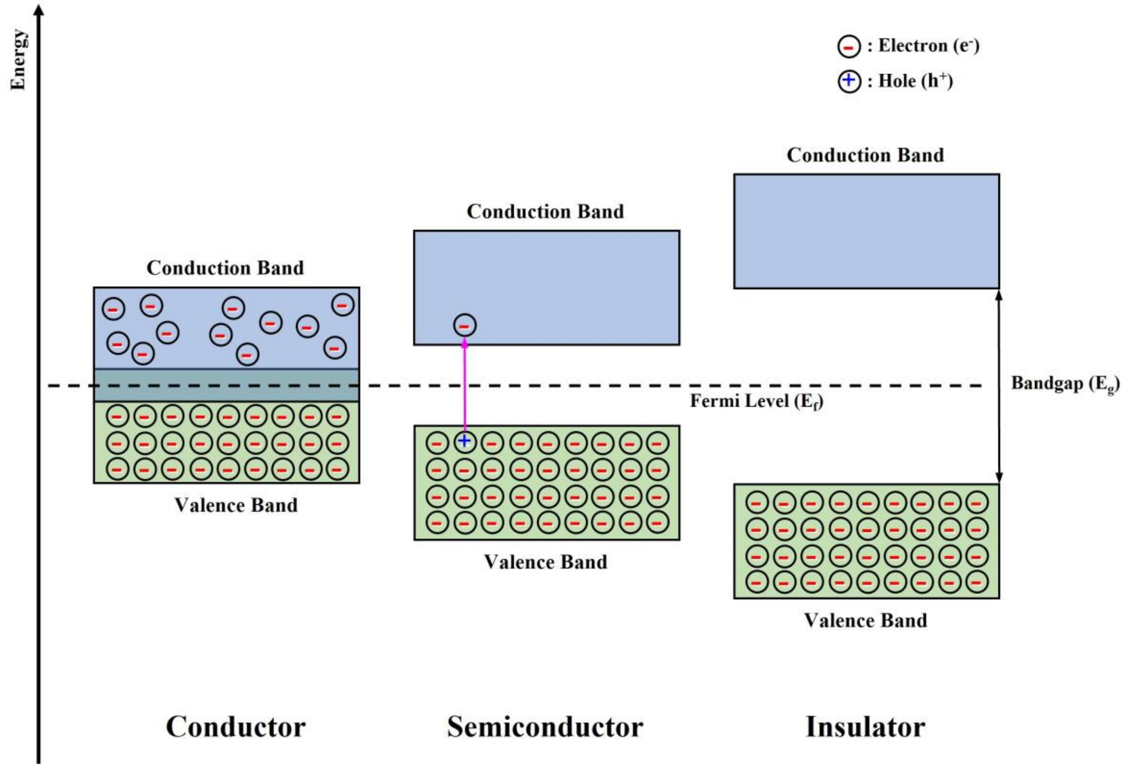

Figure 1.5 Energy band diagrams of metals (or conductor), semiconductors, and insulators

1.3.2 Structure and Operation of Dye-sensitized Solar Cell

Inorganic solar cells, used the materials such as silicon, cadmium telluride (CdTe), and copper indium gallium diselenide (CIGS), have a high energy conversion efficiency (over 20%).[25] However, inorganic solar cells are heavy, and also require high manufacturing cost compared to organic and hybrid inorganic-organic solar cells. Therefore, organic and hybrid solar cells are needed to pay more attention as alternatives. Dye-sensitized solar cells (DSSCs), are regarded as kind of organic solar cell, have been spotlighted as an alternative to the p-n junction photovoltaic cells due to their low cost, low toxicity, simple preparation, and ease of production.[26] The power conversion efficiency of DSSCs reaches up to 11% and the efficiency of laboratory cell exceeds 13%.[27] DSSCs are compose of the transparent and conductive substrate, working electrode, counter electrode, electrolyte, and dye (sensitizer). The substrate in DSSCs act as current collector. The fluorine-doped tin oxide (FTO) and indium-doped tin oxide (ITO) glasses are mostly used as transparent and conductive substrates.[28] The semiconductors such as TiO_2, ZnO, and SnO_2 are used as working electrodes or photoanodes. In particular, TiO_2 is often used due to its low toxicity and cost, and easy availability. The working electrodes are prepared by immersing dye solution for a certain time. The platinum (Pt) or carbon are used as counter electrode in DSSCs.[29, 30] The counter electrode contributes to reduce the electrolyte and to make the holes from hole transport materials.[26] The electrolytes such as I^-/I^-_3, Br^-/Br^-_2, and SCN^-/SCN_2 are mainly used in DSSCs.[31-33] In DSSCs, dye plays an key role in generating the electrons by absorbing the sunlight. The various organic, inorganic, metal-free, and natural dyes, such as N3, N719, N749, Z907, K8, K19, N945, Z910, K73, Y123, and Z907, have been used as photosensitizers in DSSCs.[34-44]

The construction and working principle of DSSCs are shown as Figure 1.6. From the sunlight, photon is absorbed by photosensitizer (dye) and the electrons move from the ground state (S^+/S) to the excited state (S^+/S^*). Then the excited electrons move to the conduction band of TiO_2 which is located below the excited state of dye. The electrons at the TiO_2 move toward FTO glass and then are transported to the counter electrode through the external circuit. Next, the electrons at the counter electrode reduce the electrolyte from I^-_3 to I^-. In other words, the electrons at the electrolyte are released to the ground state of the dye. Lastly, the I^-_3 moves back to the counter electrode and reduces to I^- ion. The reaction mechanism of DSSCs are as below.[26]

$$S^+/S + hv \rightarrow S^+/S^*$$

$$S^+/S^* \rightarrow S^+/S + e^- (TiO_2)$$

$$S^+/S^* + e^- \rightarrow S^+/S$$

$$I^-_3 + 2e^- \rightarrow 3I^-$$

1.3.3 Performance Evaluation of Dye-sensitized Solar Cell

The performance of DSSCs is evaluated by five key parameters such as short circuit current (J_{sc}, mA/cm^2), open circuit voltage (V_{oc}, V), fill factor (FF), maximum power output (P_{max}), power conversion efficiency (PCE or η, %) as shown in figure 1.7.[26]

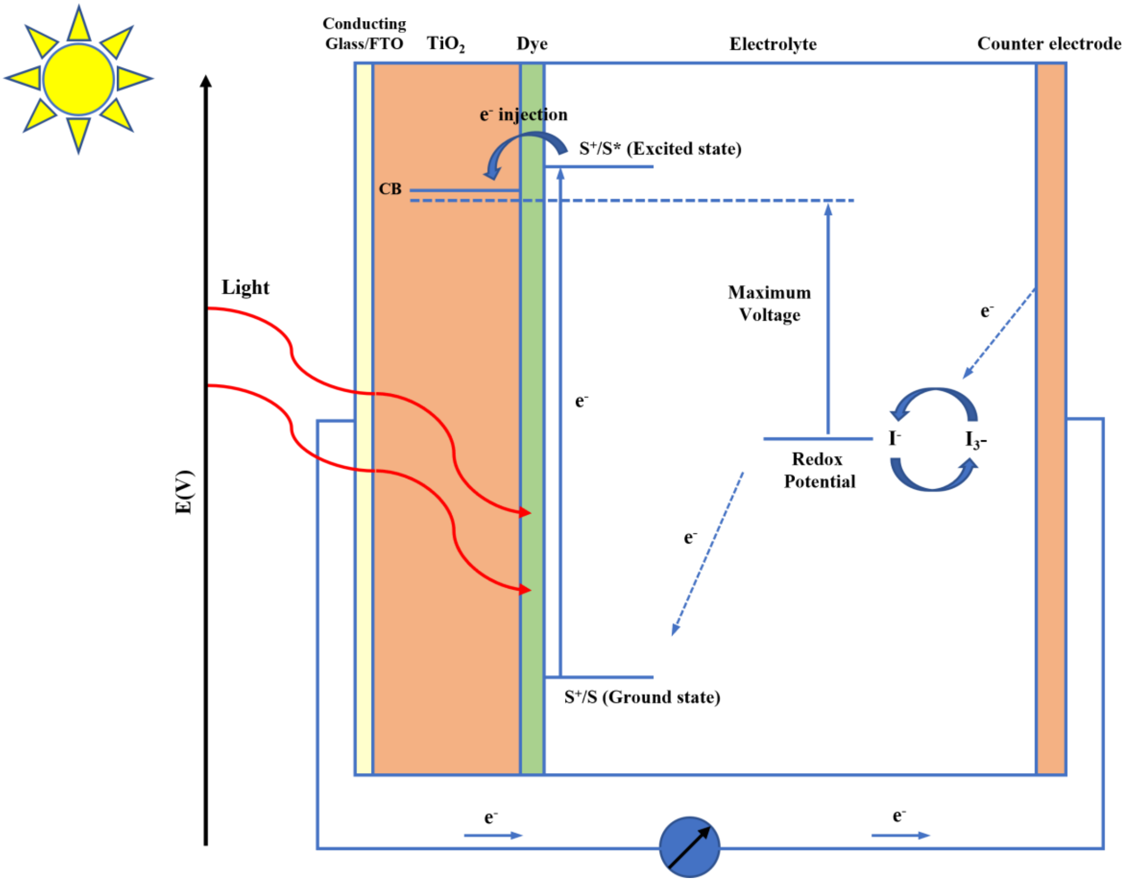

Figure 1.6 Construction and working principle of the dye-sensitized nanocrystalline solar cell.[26]

The open circuit voltage is the potential difference between positive and negative electrodes under zero current. The fill factor is inversely proportional to V_{oc} and I_{sc}, and also can be calculated by the maximum area of J-V curve or the ratio of maximum power (J_{mp} x V_{mp}) to the product (J_{sc} x V_{oc}). The expression of fill factor as shown below.

$$FF = (\text{Area B}) / (\text{Area A}) = (J_{mp} \cdot V_{mp}) / (J_{sc} \cdot V_{oc})$$

where V_{mp} and J_{mp} are the maximum voltage and current, respectively

The overall power conversion efficiency of DSSCs can be expressed as shown below.[45]

$$\eta\ (\%) = (J_{sc} \cdot V_{oc} \cdot FF) / P_{in}$$

where P_{in} is the input power, the overall efficiency is the ratio of the output power density to the input power density. the efficiency increases with increasing J_{sc}, V_{oc}, and FF.

1.4 Lithium-ion Battery Fundamental

Driven by an ever-growing demand for energy, environmental-friendly, sustainable, and renewable sources of energy have been gaining more traction as feasible solution towards meeting out future energy needs. Consistent with this trend, secondary (rechargeable) batteries are gradually replacing primary (non-rechargeable) batteries as an effective way to store energy from renewables, provide dispatchable clean power, and contribute toward reducing environmental pollution.[46] Among second batteries, lithium-ion batteries (LIBs) are one of the most advanced rechargeable battery chemistries. LIBs are widely used in portable electronics, power tools, and hybrid electric vehicles due to the outstanding properties such as high electrochemical potential (3.6V), superior energy density (250-693 $Wh \cdot L^{-1}$), and long cycle life (over 5,000 cycles). Therefore, LIBs are

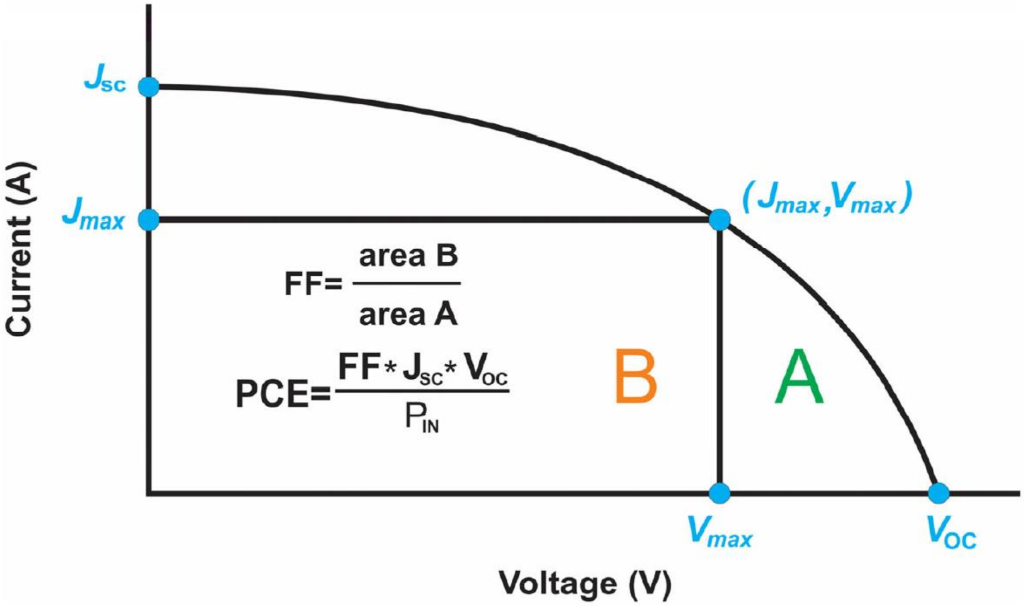

Figure 1.7 Current density-voltage characteristic (J-V curve) for DSSCs performance.[26]

currently the most promising batteries on the market for meeting our renewable energy storage needs.[46, 47]

The typical LIBs are composed of cathode, anode, separator, electrolyte, current collector, spacer, spring, and case. The traditional cathodes are $LiCoO_2$ (layered structure), $LiFePO_4$ (Olivine structure), and $LiMn_2O_4$ (Spinel structure) on aluminum substrate. Especially, cobalt oxide is expensive and has safety issues because of overcharging. The alternatives for cobalt oxide such as $LiMn_2O_4$ (LMO), $LiNi_{1/3}Mn_{1/3}Co_{1/3}O_2$ (NCM), $LiNi_{0.8}Co_{0.15}Al_{0.05}O_2$ (NCA), $LiFePO_4$ (LFP) are drawing attention. NCM and LFP are suitable candidates for large-scale batteries due to their safety and cost-effectiveness. The anodes are commonly graphite on copper substrate due to low cost, easy availability, and good electronic conductivity, but the graphite exhibits poor specific capacity and has safety issues. To supplement its drawbacks, the many different anode materials have been explored such as alloy materials (aluminum (Al), tin (Sn), magnesium (Mg), silver (Ag), antimony (Sb), and their alloys), transition metal-based compounds (iron oxide (Fe_3O_4), titanium oxide (TiO_2), molybdenum disulfide (MoS_2), zinc/manganese oxide ($ZnMn_2O_4$), titanium niobium oxide (TNO) , silicon-based compounds, and carbon-based compounds (carbon nanotubes (CNTs), graphene, and carbon spheres). The role of separator in LIBs is to prevent the physical contact between cathode and anode, causing the battery fire or explosion. The separators can be categorized by their structure or material such as microporous membrane, nonwovens, gel-polymer electrolyte, composite membranes. The materials of separator in Li-ion battery require good chemical and thermal stabilities, enough thickness and strength, proper porosity and pore size. Lastly, the electrolyte transports the lithium-ions between anode and cathode. There are five types of electrolytes including non-aqueous electrolytes, aqueous electrolytes, ionic liquids, polymer, and hybrid electrolytes. In the majority of rechargeable batteries, the non-aqueous organic electrolytes, such as lithium hexafluorophosphate ($LiPF_6$) salt with organic carbonates are currently used. The electrolytes also require good stability, non-toxicity, and low cost.[48]

Figure 1.8 shows a schematic diagram of operation mechanism of LIBs (graphite/$LiCoO_2$).[49] During the charging process, the lithium-ions de-intercalated from cathode ($LiCoO_2$) and move toward anode side (graphite) through the electrolyte. The electrons also move into the anode side via the external circuit.[50] The anodic and cathodic reaction equations during the charging process are as below.

Charging:

$$\text{Anodic reaction: } Li^+ + e^- + 6C \rightarrow LiC_6 \text{ (Reduction)}$$

$$\text{Cathodic reaction: } LiCoO_2 \rightarrow CoO_2 + Li^+ + e^- \text{ (Oxidation)}$$

The anodic and cathodic reactions during the discharging process are reverse reactions. The electrolyte and separator allow the lithium ions to easily move between anode and cathode through the pore structure of separator.

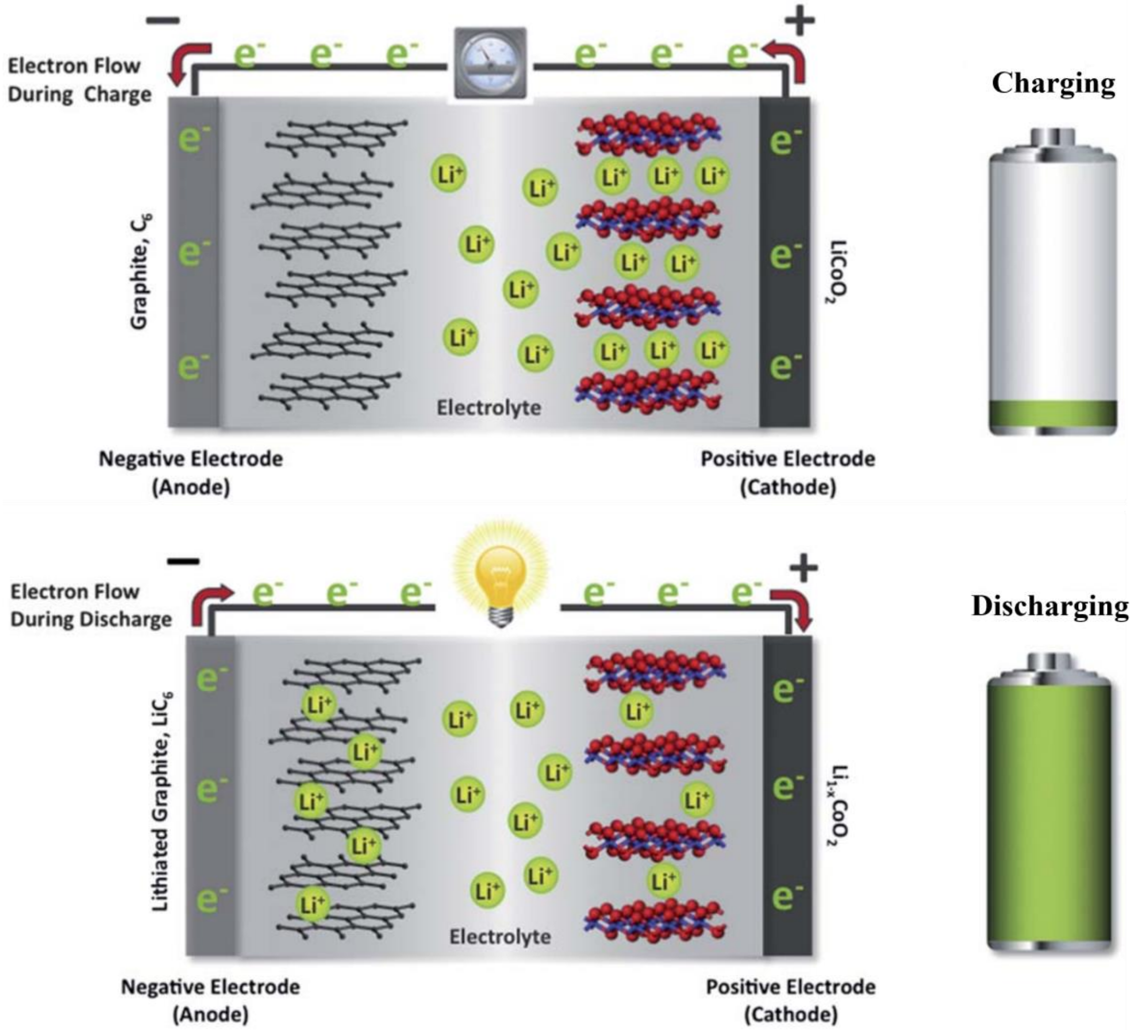

Figure 1.8 A schematic diagram of working principle of lithium-ion battery.[49]

Reference

1. INTERNATIONAL ENERGY OUTLOOK 2021 (IEO2021). *U.S. Energy Information Administration (EIA)* **2021**.
2. Stein, E. W. J. R.; Reviews, S. E., A comprehensive multi-criteria model to rank electric energy production technologies. **2013,** *22*, 640-654.
3. Patel, N. J. J. R. R. E. T., Environmental and economical effects of fossil fuels. **2014,** *1*, 1-12.
4. Fulkerson, W.; Judkins, R. R.; Sanghvi, M. K. J. S. A., Energy from fossil fuels. **1990,** *263* (3), 128-135.
5. Schaffer, L. M.; Bernauer, T. J. E. p., Explaining government choices for promoting renewable energy. **2014,** *68*, 15-27.
6. Ellabban, O.; Abu-Rub, H.; Blaabjerg, F. J. R.; reviews, s. e., Renewable energy resources: Current status, future prospects and their enabling technology. **2014,** *39*, 748-764.
7. Dincer, I.; Acar, C. J. I. J. o. E. R., A review on clean energy solutions for better sustainability. **2015,** *39* (5), 585-606.
8. Pursiheimo, E.; Holttinen, H.; Koljonen, T. J. R. E., Inter-sectoral effects of high renewable energy share in global energy system. **2019,** *136*, 1119-1129.
9. Information on https: // https://www.eia.gov/outlooks/aeo/pdf/aeo2019.pdf.
10. Nema, P.; Nema, R.; Rangnekar, S. J. R.; Reviews, S. E., A current and future state of art development of hybrid energy system using wind and PV-solar: A review. **2009,** *13* (8), 2096-2103.
11. https://www.c2es.org/content/renewable-energy/#:~:text=All%20sources%20of%20renewable%20energy,biomethane)%20are%20used%20for%20transportation.
12. U.S. Solar Photovoltaic System and Energy Storage Cost Benchmark: Q1 2020.
13. Blakers, A.; Zin, N.; McIntosh, K. R.; Fong, K. J. E. P., High efficiency silicon solar cells. **2013,** *33*, 1-10.
14. Zahedi, A. J. R.; reviews, s. e., Maximizing solar PV energy penetration using energy storage technology. **2011,** *15* (1), 866-870.

15. Gurung, A.; Qiao, Q. J. J., Solar charging batteries: advances, challenges, and opportunities. **2018,** *2* (7), 1217-1230.

16. Yang, Z.; Li, L.; Luo, Y.; He, R.; Qiu, L.; Lin, H.; Peng, H. J. J. o. M. C. A., An integrated device for both photoelectric conversion and energy storage based on free-standing and aligned carbon nanotube film. **2013,** *1* (3), 954-958.

17. Guo, W.; Xue, X.; Wang, S.; Lin, C.; Wang, Z. L. J. N. l., An integrated power pack of dye-sensitized solar cell and Li battery based on double-sided TiO2 nanotube arrays. **2012,** *12* (5), 2520-2523.

18. Knier, G. J. S. N., How do photovoltaics work. **2002**.

19. Bard, A. J. J. T. J. o. P. C., Design of semiconductor photoelectrochemical systems for solar energy conversion. **1982,** *86* (2), 172-177.

20. Roy, B.; Chakrabarty, S.; Mondal, O.; Pal, M.; Dutta, A. J. M. c., Effect of neodymium doping on structure, electrical and optical properties of nanocrystalline ZnO. **2012,** *70*, 1-7.

21. George, P.; Chowdhury, P. J. A., Complex dielectric transformation of UV-vis diffuse reflectance spectra for estimating optical band-gap energies and materials classification. **2019,** *144* (9), 3005-3012.

22. https://www.electricaltechnology.org/2019/10/difference-between-conductor-semiconductor-insulator.html.

23. https://en.wikipedia.org/wiki/Fermi_level#:~:text=In%20band%20structure%20theory%2C%20used,occupied%20at%20any%20given%20time.

24. Dharma, J.; Pisal, A.; Shelton, C. J. A. N. S., CT: PerkinElmer, Simple method of measuring the band gap energy value of TiO2 in the powder form using a UV/Vis/NIR spectrometer. **2009**, 1-4.

25. Miles, R. W.; Zoppi, G.; Forbes, I. J. M. t., Inorganic photovoltaic cells. **2007,** *10* (11), 20-27.

26. Sharma, K.; Sharma, V.; Sharma, S. J. N. r. l., Dye-sensitized solar cells: fundamentals and current status. **2018,** *13* (1), 1-46.

27. Mathew, S.; Yella, A.; Gao, P.; Humphry-Baker, R.; Curchod, B. F.; Ashari-Astani, N.; Tavernelli, I.; Rothlisberger, U.; Nazeeruddin, M.; Grätzel, M. J. N. c., Dye-sensitized solar cells with 13% efficiency achieved through the molecular engineering of porphyrin sensitizers. **2014,** *6* (3), 242-247.

28. Ye, M.; Wen, X.; Wang, M.; Iocozzia, J.; Zhang, N.; Lin, C.; Lin, Z. J. M. T., Recent advances in dye-sensitized solar cells: from photoanodes, sensitizers and electrolytes to counter electrodes. **2015,** *18* (3), 155-162.

29. Grätzel, M.; Moser, J.-E. J. E. t. i. c., Solar energy conversion. Citeseer: 2001; Vol. 5, pp 589-644.

30. Wang, H.-J.; Chen, C.-P.; Jeng, R.-J. J. M., Polythiophenes comprising conjugated pendants for polymer solar cells: a review. **2014,** *7* (4), 2411-2439.

31. Gao, F.; Wang, Y.; Shi, D.; Zhang, J.; Wang, M.; Jing, X.; Humphry-Baker, R.; Wang, P.; Zakeeruddin, S. M.; Grätzel, M. J. J. o. t. A. C. S., Enhance the optical absorptivity of nanocrystalline TiO2 film with high molar extinction coefficient ruthenium sensitizers for high performance dye-sensitized solar cells. **2008,** *130* (32), 10720-10728.

32. Ferrere, S.; Zaban, A.; Gregg, B. A. J. T. J. o. P. C. B., Dye sensitization of nanocrystalline tin oxide by perylene derivatives. **1997,** *101* (23), 4490-4493.

33. Oskam, G.; Bergeron, B. V.; Meyer, G. J.; Searson, P. C. J. T. J. o. P. C. B., Pseudohalogens for dye-sensitized TiO2 photoelectrochemical cells. **2001,** *105* (29), 6867-6873.

34. Hagfeldt, A.; Boschloo, G.; Sun, L.; Kloo, L.; Pettersson, H. J. C. r., Dye-sensitized solar cells. **2010,** *110* (11), 6595-6663.

35. Funaki, T.; Yanagida, M.; Onozawa-Komatsuzaki, N.; Kasuga, K.; Kawanishi, Y.; Sugihara, H. J. I. C. A., A 2-quinolinecarboxylate-substituted ruthenium (II) complex as a new type of sensitizer for dye-sensitized solar cells. **2009,** *362* (7), 2519-2522.

36. Bessho, T.; Constable, E. C.; Graetzel, M.; Redondo, A. H.; Housecroft, C. E.; Kylberg, W.; Nazeeruddin, M. K.; Neuburger, M.; Schaffner, S. J. C. C., An element of surprise—efficient copper-functionalized dye-sensitized solar cells. **2008,** (32), 3717-3719.

37. Onozawa-Komatsuzaki, N.; Yanagida, M.; Funaki, T.; Kasuga, K.; Sayama, K.; Sugihara, H. J. S. e. m.; cells, s., Near-IR dye-sensitized solar cells using a new type of ruthenium complexes having 2, 6-bis (quinolin-2-yl) pyridine derivatives. **2011,** *95* (1), 310-314.

38. Onozawa-Komatsuzaki, N.; Yanagida, M.; Funaki, T.; Kasuga, K.; Sayama, K.; Sugihara, H. J. I. C. C., Near-IR sensitization of nanocrystalline TiO2 with a new ruthenium complex having a 2, 6-bis (4-carboxyquinolin-2-yl) pyridine ligand. **2009,** *12* (12), 1212-1215.

39. White, R. C.; Benedetti, J. E.; Gonçalves, A. D.; Romão, W.; Vaz, B. G.; Eberlin, M. N.; Correia, C. R.; De Paoli, M. A.; Nogueira, A. F. J. J. o. P.; Chemistry, P. A., Synthesis, characterization and introduction of a new ion-coordinating ruthenium sensitizer dye in quasi-solid state TiO2 solar cells. **2011,** *222* (1), 185-191.

40. Sivakumar, R.; Marcelis, A. T.; Anandan, S. J. J. o. P.; Chemistry, P. A., Synthesis and characterization of novel heteroleptic ruthenium sensitizer for nanocrystalline dye-sensitized solar cells. **2009,** *208* (2-3), 154-158.

41. Kuang, D.; Ito, S.; Wenger, B.; Klein, C.; Moser, J.-E.; Humphry-Baker, R.; Zakeeruddin, S. M.; Grätzel, M. J. J. o. t. A. C. S., High molar extinction coefficient heteroleptic ruthenium complexes for thin film dye-sensitized solar cells. **2006,** *128* (12), 4146-4154.

42. Sahin, C.; Ulusoy, M.; Zafer, C.; Ozsoy, C.; Varlikli, C.; Dittrich, T.; Cetinkaya, B.; Icli, S. J. D.; Pigments, The synthesis and characterization of 2-(2′-pyridyl) benzimidazole heteroleptic ruthenium complex: Efficient sensitizer for molecular photovoltaics. **2010,** *84* (1), 88-94.

43. Ahmad, S.; Bessho, T.; Kessler, F.; Baranoff, E.; Frey, J.; Yi, C.; Grätzel, M.; Nazeeruddin, M. K. J. P. C. C. P., A new generation of platinum and iodine free efficient dye-sensitized solar cells. **2012,** *14* (30), 10631-10639.

44. Tsao, H. N.; Burschka, J.; Yi, C.; Kessler, F.; Nazeeruddin, M. K.; Grätzel, M. J. E.; Science, E., Influence of the interfacial charge-transfer resistance at the counter electrode in dye-sensitized solar cells employing cobalt redox shuttles. **2011,** *4* (12), 4921-4924.

45. Murakami, T. N.; Grätzel, M. J. I. C. A., Counter electrodes for DSC: application of functional materials as catalysts. **2008,** *361* (3), 572-580.

46. Soylu, S., *Electric vehicles: the benefits and barriers*. BoD–Books on Demand: 2011.

47. https://en.wikipedia.org/wiki/Lithium-ion_battery.

48. Li, Q.; Chen, J.; Fan, L.; Kong, X.; Lu, Y. J. G. E.; Environment, Progress in electrolytes for rechargeable Li-based batteries and beyond. **2016,** *1* (1), 18-42.

49. Thackeray, M. M.; Wolverton, C.; Isaacs, E. D. J. E.; Science, E., Electrical energy storage for transportation—approaching the limits of, and going beyond, lithium-ion batteries. **2012,** *5* (7), 7854-7863.

50. Yao, Y., Carbon based anode materials for lithium-ion batteries. **2003**.

Chapter 2. Integrating Photovoltaic and Energy Storage Systems in One Device

2.1 Introduction

The traditional or conventional PV-battery system is that solar PV system and battery system are independently connected by external wires. The $Li_4Ti_5O_{12}$-$LiCoO_2$ battery is charged by perovskite solar cell (PSC) and dye-sensitized solar cell (DSSC) through DC-DC voltage booster converter as shown in Figure 2.1.[1] The DC-DC booster converter is employed to meet the voltage requirement for charging the battery. The Furthermore, DSSC and PSC are connected with battery or capacitor through converters in other literatures.[2-4] The integrated solar PV-battery systems are largely categorized by the circuit structure. Based on the circuit structure, there are two different configurations depending on the number of electrodes. Between two and three electrode systems, three electrodes system especially possesses a tandem structure, which has stacked the individual electrodes. Another way to classify the integrated solar PV-battery is by the system design and working principle. In Figure 2.2, three different types of integrated solar batteries, such as direct integration, photo-assisted integration, and redox flow battery integration are represented.[5-7] Direct integration is composed of the stacked electrodes, which are working independently without external wires between solar cell and battery. In Photo-assisted integration, PV cell and battery are also integrated together, and photo-assisted charging is effective to assist the battery. The major purpose of photo-assisted charging is to lower high charging voltage of the battery. Redox flow integration

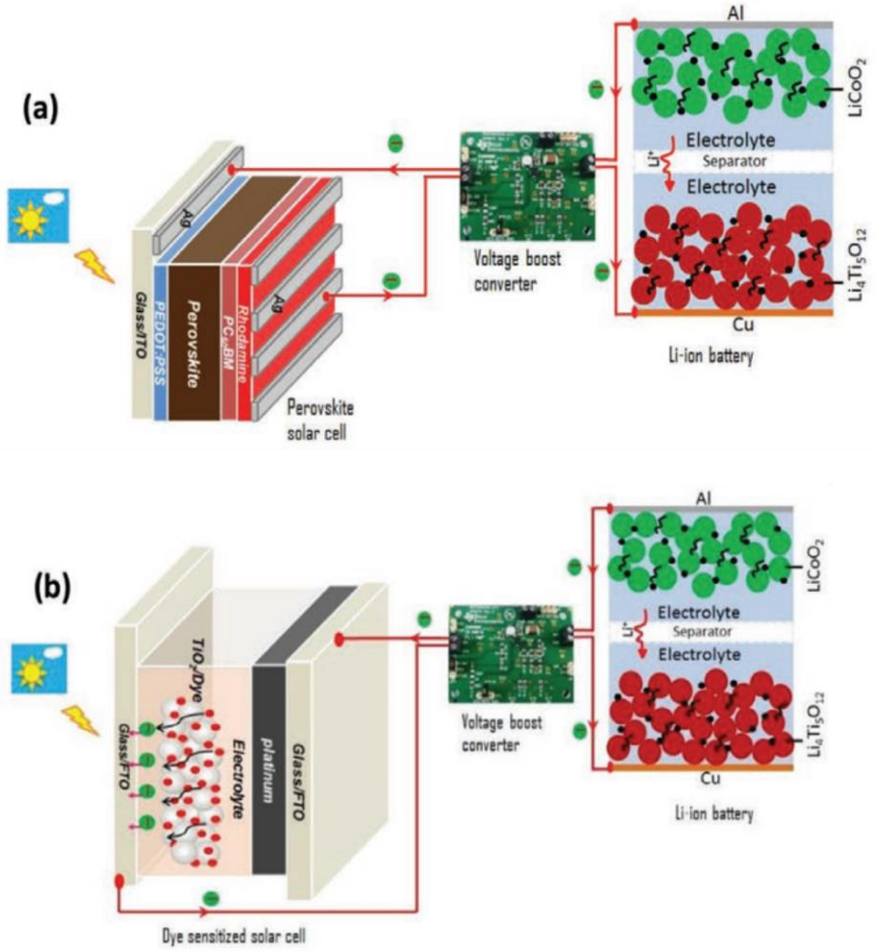

Figure 2.1 Photocharging diagram of $Li_4Ti_5O_{12}$-$LiCoO_2$ cell using (a) perovskite solar cells and (b) dye-sensitized solar cells.[1]

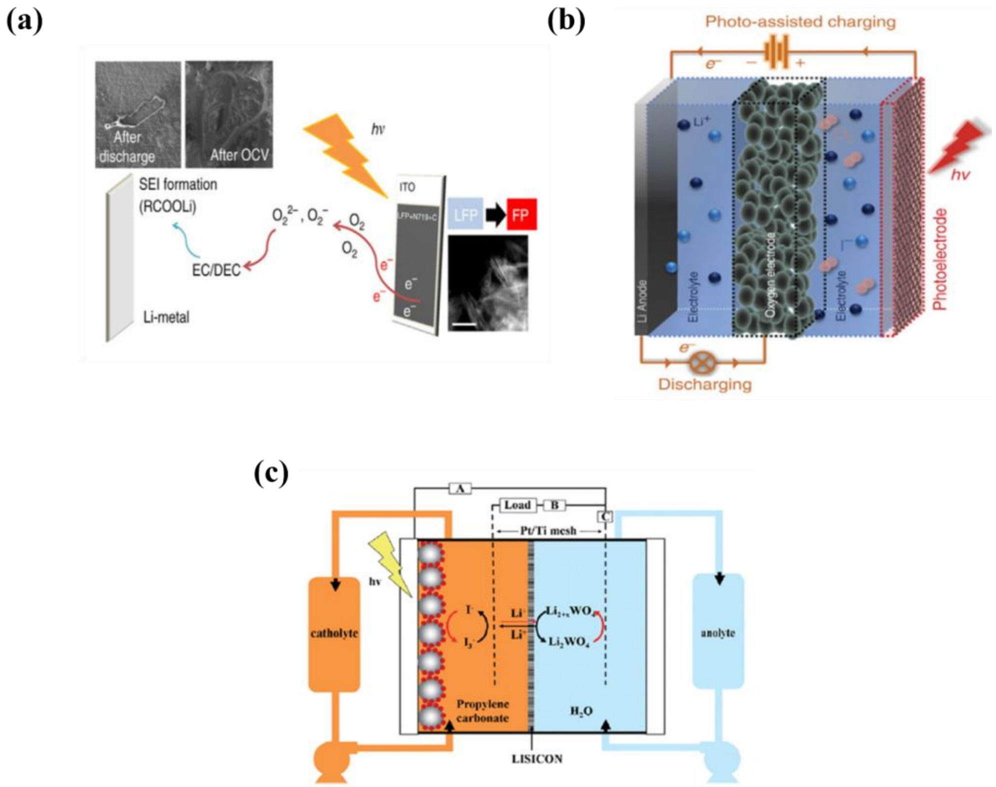

Figure 2.2 Categorization of PV-battery by a system design (a) Direct integration, (b) photo-assisted integration, and (c) redox flow battery integration.[5-7]

is that redox flow battery is combined with photocharging. A typical redox flow battery is composed of two tanks of electrolytes based on a membrane and can be recharged by replacing the electrolytes. The electricity production depends on the total volume of electrolytes in the tanks.

The direct integrated PV-battery system, consists of two-electrode structures, can be compared to our system due to the similarity of circuit structure and system design. There are only few reports for such system in the literature. Direct-integrated PV-battery system including two electrodes was recently introduced by photo-oxidation of cathode ($LiFePO_4$ with N719 dye) as shown in Figure 2.2.(a).[6] Li metal and 1M $LiPF_6$ with EC/DEC were used as an anode and electrolyte, respectively. The electron-hole pairs were produced by sensitizing dye with sunlight and the holes allow $LiFePO_4$ to form FePO4 through delithiation process. The overall efficiency of LFP/CNTs/N719 reached to the range of 0.06-0.08% and the discharge capacity of around 340 mAh/g at C/24 was established under illumination during discharge process. Shahab et al. reported that perovskite photo-batteries are demonstrated by using highly photoactive two-dimensional lead halide perovskite, which can perform both photocharging and energy storage simultaneously in the device as shown in Figure 2.3.(a).[8] This device has Cu | perovskite | separator and electrolyte | Li | SS | Al layers. 1M $LiPF_6$ and borosilicate paper were used as electrolyte and separator, respectively. Jiangquan et al. demonstrated that a covalent organic framework integrating naphthalene diimide and triphenylamine (NT-COF). NT-COF and Li metal were employed as cathode and anode for direct solar to energy conversion and storage as shown in Figure 2.3.(b).[9] Such system achieved up to ~124

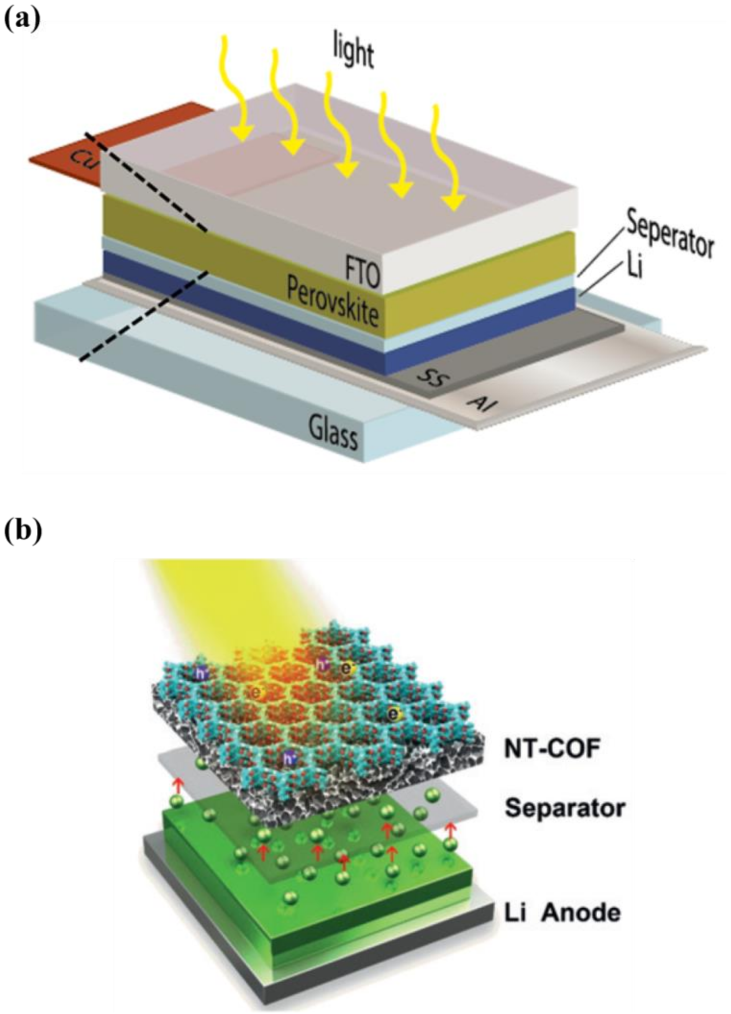

Figure 2.3 Direct integrated PV-Battery system with two electrodes.[8, 9]

mAh/g, which corresponds to the 96% of theoretical capacity. In addition, the efficiency of battery under illumination increased 38.7% compared to the efficiency in the dark.

We invented a unique concept for a direct integrated photo-rechargeable battery, which combines solar production with an energy storage system in a single device. Our photo-rechargeable battery has the potential to bring considerable advantages in renewable energy and energy storage applications by simplifying the device architecture while minimizing energy losses. Most of their published systems are not real photo-rechargeable batteries because they also connect a solar cell and a battery in a tandem configuration. As a result, they are still unable to address the basic issues with traditional solar energy production and energy storage architecture. Our solar battery demonstrates actual solar cell and battery properties at the same time, and its complementing architecture and characteristics address typical drawbacks of systems, especially the imbalance between energy demand and supply. The overproduction of electric power in a normal solar PV system requires the use of an extra storage system. The solar battery has a layered structure, which is composed of photoelectrode, electrolyte, and cathode as shown in Figure 2.4. Titanium dioxide (TiO_2) and lithium iron phosphate ($LiFePO_4$) are used as photoanode and cathode, respectively.

The photo-charging procedure of the solar battery is as follows:

At the photoanode side,

$$TiO_2 + hv \rightarrow TiO_2^*$$

$$Ti(IV)O_2^* + Li^+ \rightarrow LiTi(III)O_2 + h^+$$

At the cathode side,

$$LiFe(II)PO_4 + h^+ \rightarrow Fe(III)PO_4 + Li^+$$

Based on the procedure above, the Li-ion from the cathode is intercalated to the photoanode during the charging. The discharging is the opposite direction. Figure 2.5 depicts the charging/discharging process of solar battery.

2.2 Chemical and Materials

FTO (Fluorine-doped Tin Oxide) glass (surface resistivity ~ 13Ω/sq, Sigma Aldrich), titania paste (Sigma Aldrich), lithium iron phosphate (LFP, MTI corporation), conductive carbon black (super P, MTI corporation), propylene carbonate (PC, Sigma Aldrich, 99.7%), lithium bis-trifluoromethanesulfonimide (LiTFSi, Sigma Aldrich), 1-methyl-2-pyrrolidinone (NMP, Fisher Scientific, 99%), polyvinylidene fluoride (PVDF, Sigma Aldrich, Mw ~ 534,000 $g\cdot cm^{-1}$), chloroplatinic acid hexahydrate (Sigma Aldrich), lithium iodide (LiI, Sigma Aldrich), Iodine (I_2, Sigma Aldrich, 99.8%), 4-tert-Butylpyridine (Sigma Aldrich, 98%), guanidine thiocyanate (Sigma Aldrich, 99%), valeronitrile (Sigma Aldrich, 99.5%), acetonitrile (Sigma Aldrich, 99.8%), surlyn film (Solaronix, 60μm thickness), epoxy glue, were purchased.

2.3 Apparatus and Equipment

Linear sweep voltammetry (LSV), chrono-amperometry, cyclic voltammetry (CV), charging and discharging test were measured by potentiostat/galvanostat (VersaSTAT 4, AMETEK) to determine the performance and characteristic of fabricated

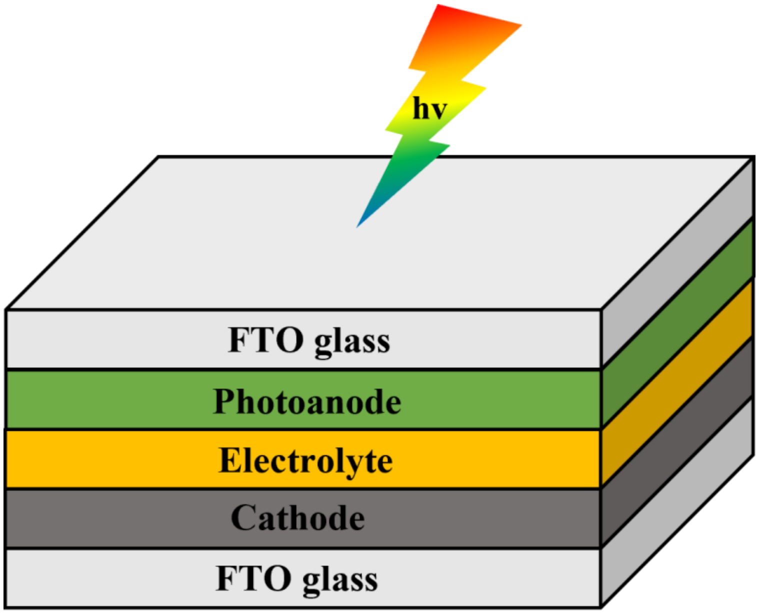

Figure 2.4 Layered structure of developed photo-rechargeable battery

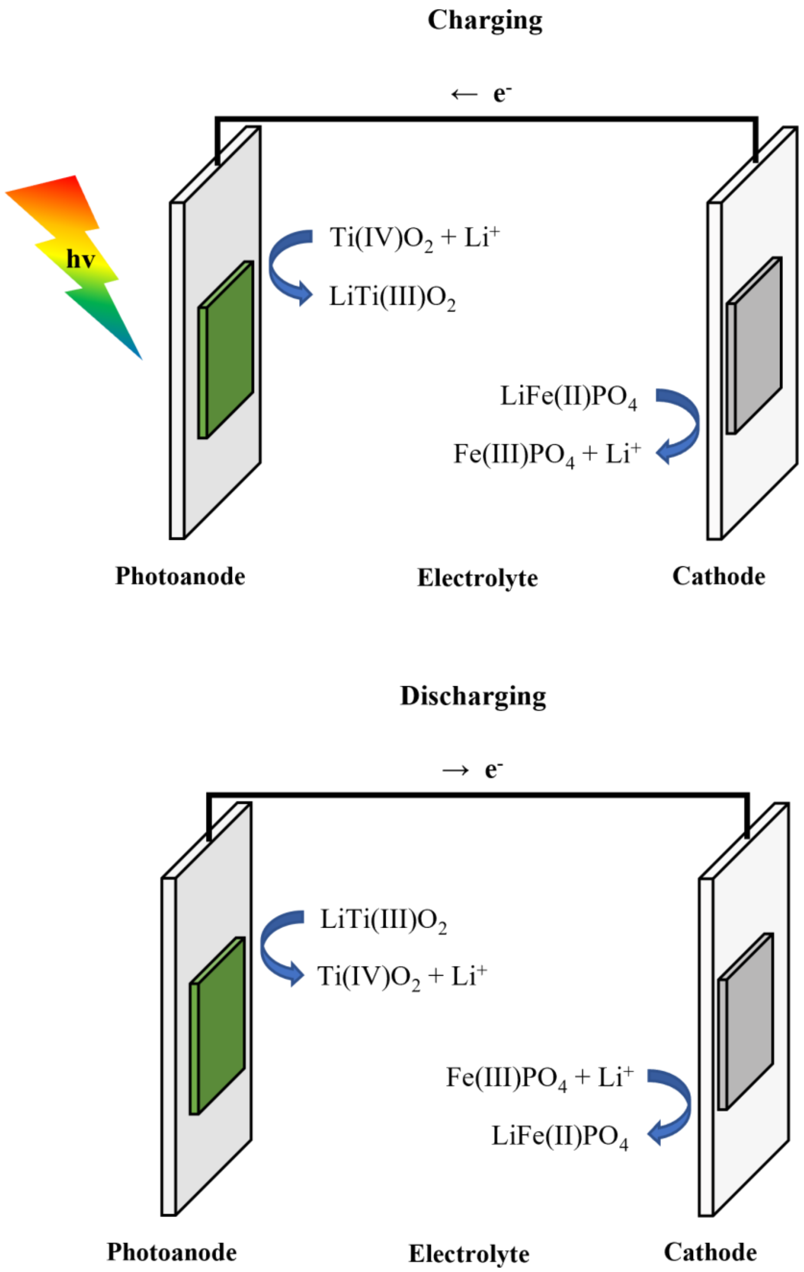

Figure 2.5 Schematic diagram of charging and discharging process

solar battery. A solar simulator (Newport, Oriel Sol3A Class AAA Solar Simulator, 450 W Xenon) was used for the light source (AM 1.5G, 100mW· cm^{-2}). The solar simulator was calibrated by a monoclinic silicon solar cell (Newport, Oriel Reference Solar Cell & Meter, 91150V).

2.4 Cell Preparation

2.4.1 Electrode Preparation

FTO glass substrate with size of (2 cm X 2 cm) was cleaned in ultrasonic bath using the detergent in deionized (DI) water, acetone, and isopropyl alcohol (IPA) in this order with ultrasonication for 5 minutes and then the nitrogen spray gun was employed to dry and clean the FTO glass. 50 mM chloroplatinic acid hexahydrate in ethanol was prepared and was spin-coated at 2000 rpm for 30 seconds on FTO glass substrate as a counter electrode for linear sweep voltammetry (LSV), electrochemical impedance spectroscopy (EIS), and chrono-amperometry tests. In open-air environment, the deposited layer was sintered in muffle furnace at 400°C for 30 minutes. For the preparation of TiO_2 photoanode, titania paste was casted on the FTO glass by doctor blading and the electrode thickness was determined by thickness of Kapton tape (40μm). Then the Kapton tape was removed, and the deposited electrode was annealed at 550°C for 30 min in the box furnace to have the transparent TiO_2 electrode layer. LFP, PVDF, and carbon black were measured and blended in an 8:1:1 weight ratio for the cathode preparation. The powders were put into the vial with NMP solvent, and the mixture was stirred for overnight. To construct the cathode layer, the well-mixed slurry was casted on the FTO glass with 40μm thickness and then the cathode was dried in the oven at 120°C overnight.

2.4.2 Electrolyte Preparation

For the full cell tests, 1M of LiTFSi was completely dissolved in PC. The mixture was stirred at room temperature to have a transparent electrolyte solution. The electrolyte solution for the half cell experiments was made up of 0.05 M LiI, 0.03 M I_2, 0.5 M 4-tert-Burylpyridine, and 0.1 M guanidine thiocyanate in a mixture of valeronitrile and acetonitrile solvent (1:1 v/v).

2.4.3 Cell Assembly

For the full cell assembly, the prepared photoanode (TiO_2) and cathode (LFP) were stacked and sealed with a surlyn film between the two electrodes. After that, the stacked electrodes were heated in the oven at 120°C for 4 minutes to melt the film. The 1M LiTFSi with PC electrolyte was injected into the device through the crevice of the surlyn film in the glovebox. An epoxy glue was utilized to seal and prevent oxygen and moisture from reacting with internal components of solar battery during the operation. The fabrication procedure of solar battery is shown in Figure 2.6.

2.5 Results and Discussions

2.5.1 Linear Sweep Voltammetry (LSV)

LSV, representing the current vs. potential, is one of the voltametric methods that

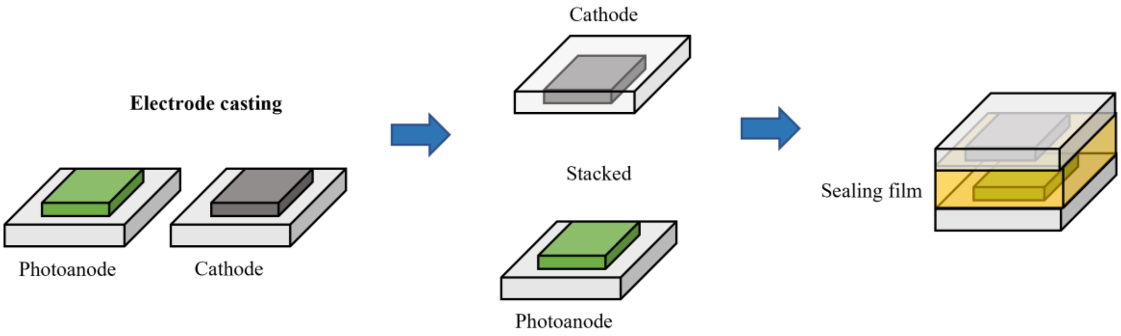

Figure 2.6 Fabrication procedure for direct integrated photo-rechargeable battery

measure the current at a working electrode as a function of voltage per time and scan rate by linearly sweeping the potential between the working and counter electrodes. Figure 2.7 shows the J-V characteristics curves for solar battery. Based on the LSV curves, the efficiency of energy conversion can be calculated. A short-circuit current (I_{sc}), an open circuit potential (V_{oc}), and a fill factor (FF), maximum power output (P_{max}), and power conversion efficiency (PCE or η, %) are calculated by using the equations mentioned in Chapter 1.3.3. Compared to the solar battery in the dark, the solar battery under illumination shows improved photovoltaic performance. The values of the Voc, Jsc, P_{in}, and FF under illumination are 0.58 V, 0.38 mA/cm^2, 100 W/cm^2, and 0.59, respectively. Based on the calculation. the efficiency of energy conversion is 0.133%.

2.5.2 Chronoamperometry

Chronoamperometry is the analysis of the current in relation to the time of the fabricated device. When light pass through the fabricated cell, it generates photocurrent, and the maximum generated photocurrent is measured for 60 sec on and off cycles. The photo-current stability of the constructed device is investigated using this characteristic measurement.[10] Figure 2.8 exhibits the current density vs. time graph at light on and off irradiation condition of solar battery. The photocurrent increases from 0.0007 to 0.41 mA/cm^2 when the light is on. For 360 sec, the photocurrent is highly stable, indicating that catalytic activity at the photoelectrode influences the photocurrent. Rectangular pulses are used to evaluate photoelectrochemical stability at the interface between photoelectrode and electrolyte.

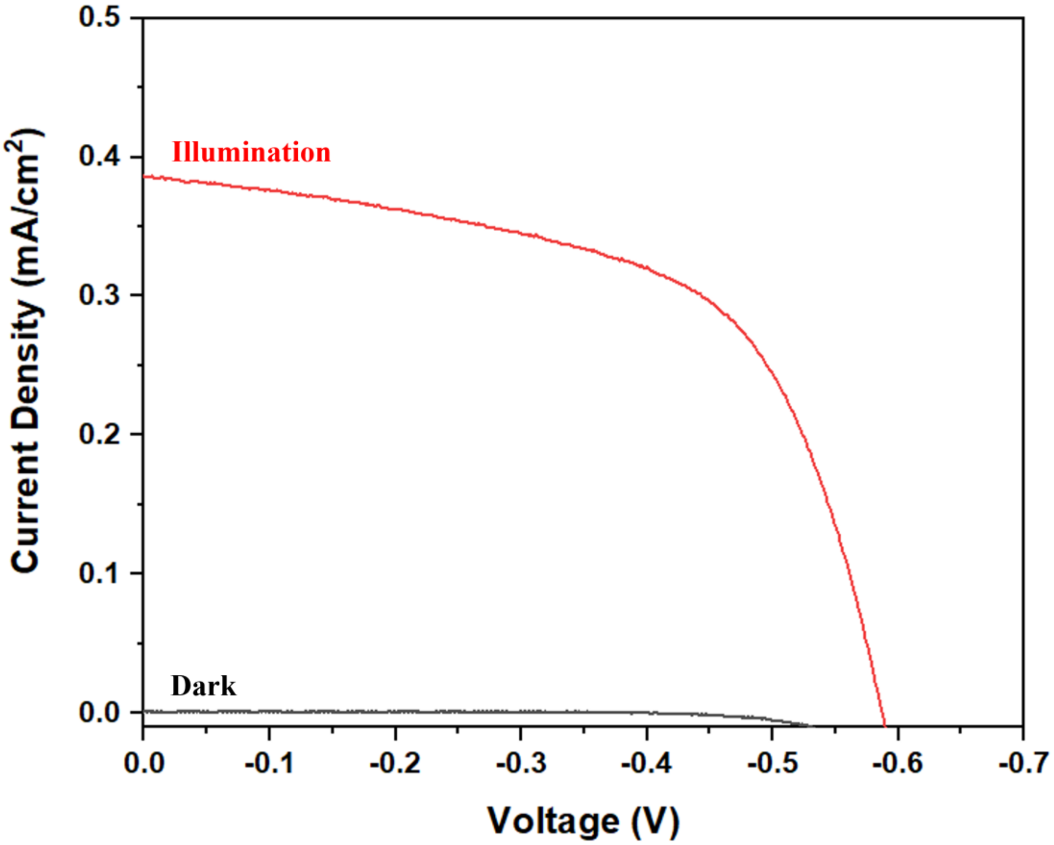

Figure 2.7 Current-voltage characteristics of solar battery in dark and under illumination

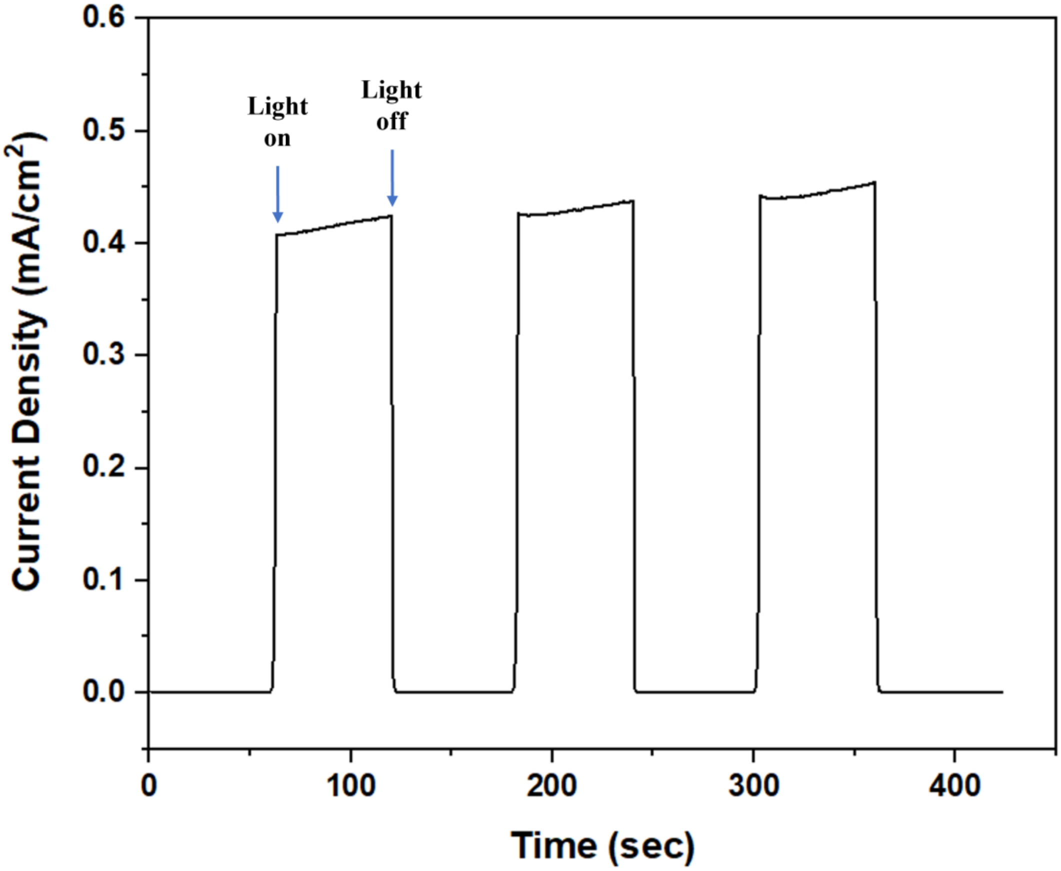

Figure 2.8 Chronoamperometry for solar battery illumination with light on and off in the 60 sec range

2.5.3 Cyclic Voltammetry (CV)

One of the most frequent electrochemical techniques is CV, which measures the current response verses a scanning potential at the interface of the working electrode and the electrolyte to better understand redox reaction processes or do quantitative analysis. Figure 2.9 shows CV curve of solar battery with different scan rates. Anodic peaks were observed at between 2.25V and 1.85V and cathode peaks locate at between 1.1V and 0.7V. This corresponds to the following reaction:

$$\text{Oxidation: } Fe^{2+} \rightarrow Fe^{3+} + e^{-}$$

$$\text{Reduction: } Ti^{4+} + e^{-} \rightarrow Ti^{3+}$$

$$LiFePO_4 + TiO_2 \leftrightarrow FePO_4 + LiTiO_2$$

Upon charging, Li^+ ion from LFP is deintercalated and dissolves into the electrolyte. TiO_2 accept electrons and reduced to Ti^{3+}. The discharge process contains the reverse reactions.

2.5.4 Charging and Discharging Test

The solar battery shows the characteristics of a solar cell and battery simultaneously. The solar battery was charged and discharged to investigate cyclic performance, ranging from 2 V to 1.2 V at a constant current of 0.1 C, as shown in Figure 2.10. A cut-off voltage is set by defining the limit value based on the CV test. Based on the ratio of charging capacity and discharging capacity, both Coulombic efficiency (CE) of the solar battery in the dark and under illumination are around 100 %. The specific discharging capacity of the solar battery under illumination is 9.6% higher than that of

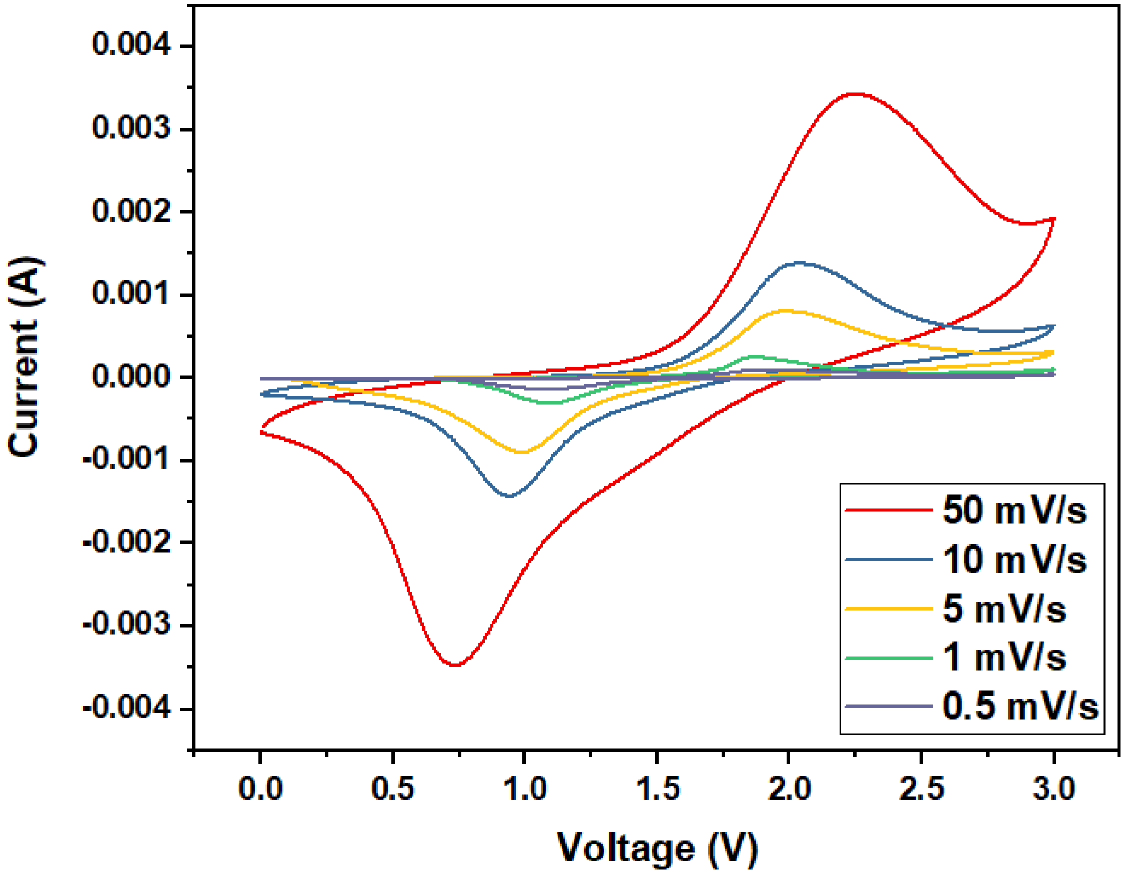

Figure 2.9 Cyclic voltammetry for solar battery with different scan rates.

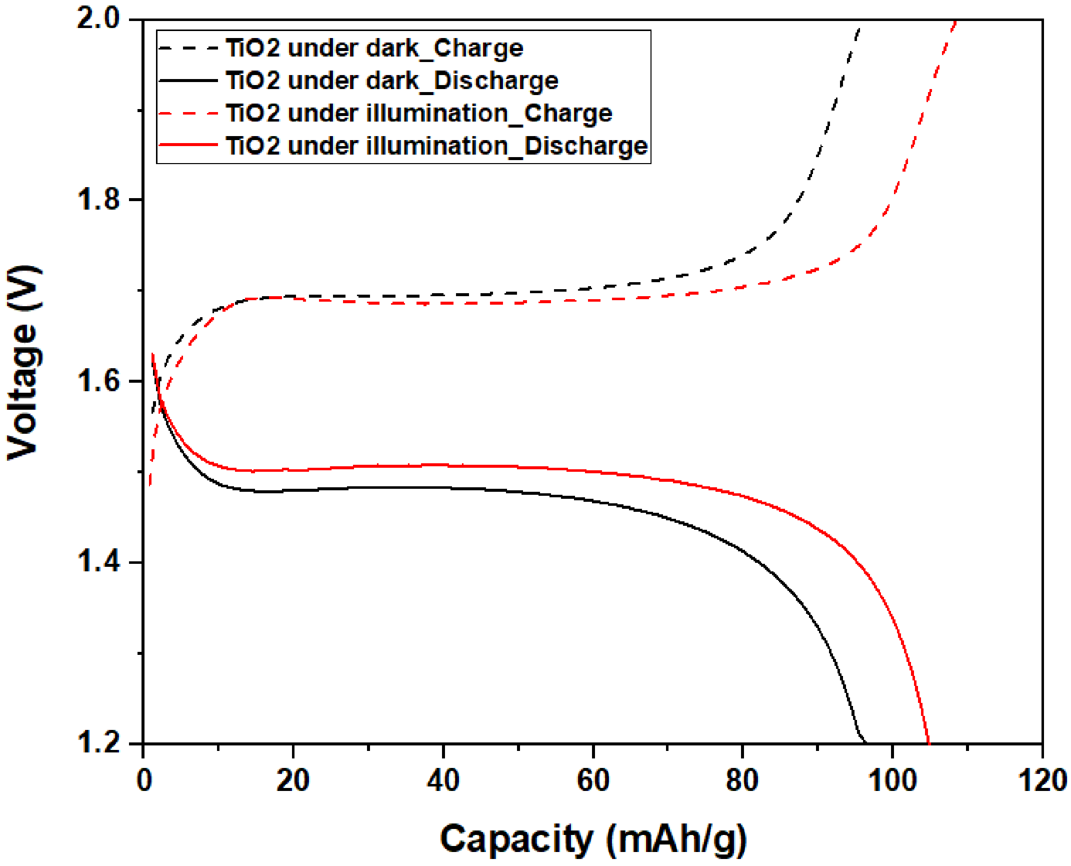

Figure 2.10 Cyclic performance test of solar battery in the dark and under illumination at 0.1 C rate.

the solar battery in dark conditions.

2.6 Conclusion

The innovative photo-rechargeable battery is invented by integrating photovoltaic and energy storage systems in one device. The characteristics of the photo-rechargeable battery are investigated by LSV, chronoamperometry, CV, and charging and discharging test. J-V characteristics exhibit that the TiO_2 photoanode in the solar battery shows high photocurrent density under illumination compared to the solar battery under dark conditions. Based on the chronoamperometry graph, the stability of the solar battery was evaluated for 360 seconds. The photocurrent density increased and was kept under illumination at intervals of 60 seconds. CV measurements determined the redox reaction peaks and the cut off voltages for cycling test was investigated as well. In addition, the specific discharging capacity of the solar battery under illumination is improved quite a lot compared to that of the solar battery under dark. The performance improvement of the solar battery using GQDs and dye will be discussed in Chapter 4.

Reference

1. Gurung, A.; Chen, K.; Khan, R.; Abdulkarim, S. S.; Varnekar, G.; Pathak, R.; Naderi, R.; Qiao, Q. J. A. E. M., Highly efficient perovskite solar cell photocharging of lithium ion battery using DC–DC booster. **2017,** *7* (11), 1602105.

2. Scalia, A.; Bella, F.; Lamberti, A.; Bianco, S.; Gerbaldi, C.; Tresso, E.; Pirri, C. F. J. J. o. P. S., A flexible and portable powerpack by solid-state supercapacitor and dye-sensitized solar cell integration. **2017,** *359*, 311-321.

3. Wu, H.; Sun, K.; Chen, R.; Hu, H.; Xing, Y. J. I. T. o. P. E., Full-bridge three-port converters with wide input voltage range for renewable power systems. **2012,** *27* (9), 3965-3974.

4. Kin, L.-c.; Liu, Z.; Astakhov, O.; Agbo, S. N.; Tempel, H.; Yu, S.; Kungl, H.; Eichel, R. d.-A.; Rau, U.; Kirchartz, T. J. A. A. E. M., Efficient Area Matched Converter Aided Solar Charging of Lithium Ion Batteries Using High Voltage Perovskite Solar Cells. **2019,** *3* (1), 431-439.

5. Yu, M.; Ren, X.; Ma, L.; Wu, Y. J. N. c., Integrating a redox-coupled dye-sensitized photoelectrode into a lithium–oxygen battery for photoassisted charging. **2014,** *5* (1), 1-6.

6. Paolella, A.; Faure, C.; Bertoni, G.; Marras, S.; Guerfi, A.; Darwiche, A.; Hovington, P.; Commarieu, B.; Wang, Z.; Prato, M. J. N. c., Light-assisted delithiation of lithium iron phosphate nanocrystals towards photo-rechargeable lithium ion batteries. **2017,** *8* (1), 1-10.

7. Yan, N.; Li, G.; Gao, X. J. J. o. M. C. A., Solar rechargeable redox flow battery based on Li 2 WO 4/LiI couples in dual-phase electrolytes. **2013,** *1* (24), 7012-7015.

8. Ahmad, S.; George, C.; Beesley, D. J.; Baumberg, J. J.; De Volder, M. J. N. l., Photo-rechargeable organo-halide perovskite batteries. **2018,** *18* (3), 1856-1862.

9. Lv, J.; Tan, Y. X.; Xie, J.; Yang, R.; Yu, M.; Sun, S.; Li, M. D.; Yuan, D.; Wang, Y. J. A. C., Direct Solar-to-Electrochemical Energy Storage in a Functionalized Covalent Organic Framework. **2018,** *130* (39), 12898-12902.

10. Kadam, V.; Jagtap, C.; Alshahrani, T.; Khan, F.; Khan, M. T.; Ahmad, N.; Al-Ahmed, A.; Pathan, H. J. J. o. M. S. M. i. E., Influence of CdS sensitization on the photovoltaic performance of CdS: TiO2 solar cell. **2021,** *32* (24), 28214-28222.

Chapter 3. Selective Synthesis of Oxidized Graphene Quantum Dots

3.1 Introduction

Graphene quantum dots (GQDs), are chemically similar to graphene oxide, have the same structure of graphene with small dimension (< 30nm).[1] The dimensions of unit cell in GQDs are a = b = 2.456 Å, c = 6.694 Å respectively. The length of bond between carbons in the bulk form is 1.418 Å, and the interlayer spacing is 3.347 Å for few layered GQDs as shown in Figure 3.1.[2, 3] GQDs also represent single layered to few layered of planar sheets formed by sp^2 hybridized carbon atoms.[4] Three electrons of 4 valence electrons in carbon atom make sigma-bond to form the hexagonal structure and the remaining one electron constitutes π-conjugation structure.[3]

GQDs have both the properties of graphene (or graphene oxide) and quantum dots such as high surface area, high transport mobility, excellent thermal/chemical stability, good solubility in water for hydroxyl and carboxyl groups at the edge of GQD, quantum confinement, and edge effect.[5] In particular, quantum confinement can be observed if the size of the material is less than its de Broglie wavelength of the electron wave function.[6] It was reported that the significant quantum confinement result in special electronic behavior if the size of graphene sheets is less than 100 nm.[7] Therefore, GQDs exhibit excellent quantum confinement effect since the movement of internal electrons are restricted to specific directions.[8, 9] Their electronic and optical properties are determined by their different size, shape, and functionalization. Graphene is known to be a zero-

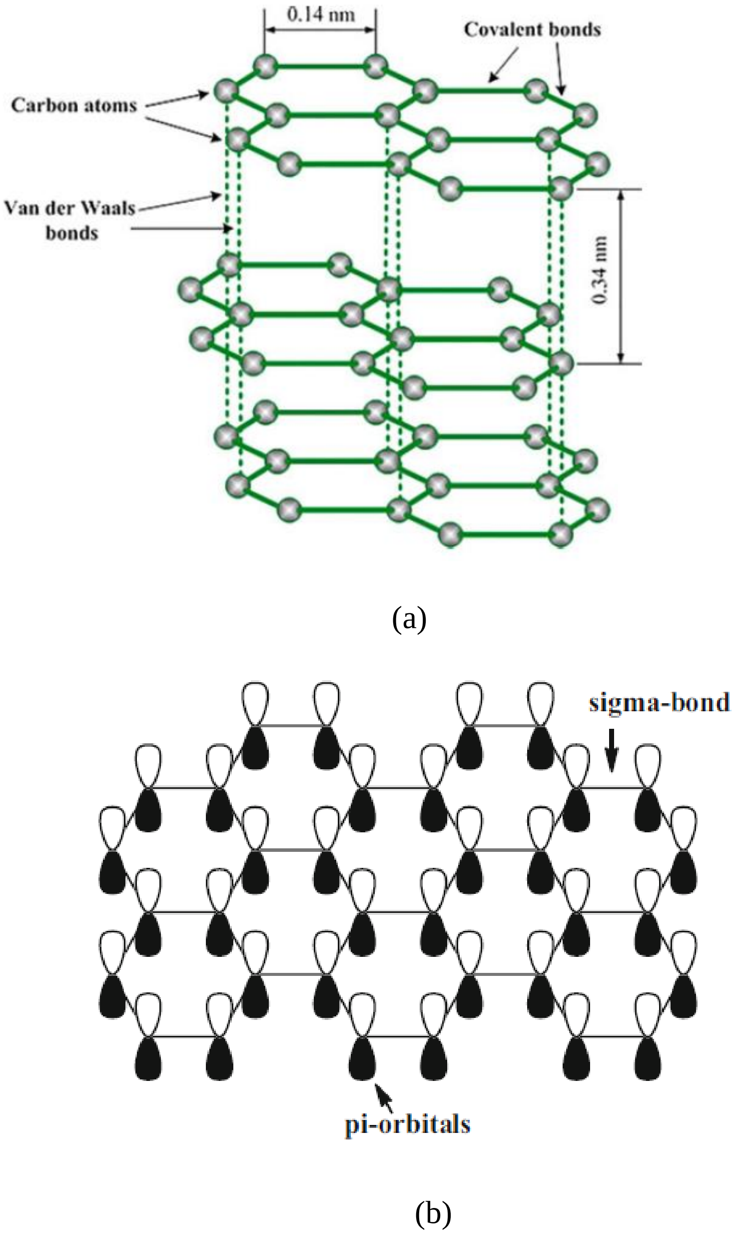

(a)

(b)

Figure 3.1 Structure of (a) graphite and (b) graphene.[3]

bandgap semiconductor. The absence of bandgap has hindered its use in electronic and optical applications.[10] On the other hand, GQDs has a tunable bandgap due to quantum confinement effect. The bandgap of GQD decreases with increasing the number of aromatic rings.[11] Furthermore, the electronic properties are also influenced by the edge types (i.e., zigzag or armchair) and shapes (e.g., round, triangular, rectangular, and hexagon).[12-15]

As highly efficient fluorescent materials, GQDs have a variety of remarkable properties, including tunable PL emission, excellent biocompatibility, low toxicity, and good photo-induced electron transfer.[16] Therefore, they have been used in many advanced applications, such as catalyst, sensors, drug delivery, bio-imaging, solar-cell, supercapacitor, batteries, and other uses.[17-22]

The strategies for obtaining GQDs are to control their size, the type and degree of functionalization, and the type of edge (Armchair or Zigzag).[23] The main approaches of GQDs can be generally classified according to the strategy applied (bottom-up or top-down approach).[24] Top-down approaches refer to the breaking down of the bulk materials (coal, graphene, graphite, graphene oxide, carbon black, carbon fiber, and CNT) gradually into a small size by chemical ablation, electrochemical oxidation, oxygen plasma treatment, thermal decomposition, combustion oxidation, and laser ablation.[25-29] Bottom-up approach aims to build materials from atom or small molecules to larger structures. GQDs are synthesized through polymerization of molecule precursors (glucose, sucrose, gelatin, citric acid) by microwave method, hydrothermal method, solvothermal method, pyrolysis/carbonization, and chemical vapor deposition (CVD).[30-34]

In this chapter, we suggest the new post-treatment method to remove sodium hydroxide (NaOH) and to selectively collect oxidized GQDs simultaneously synthesized by electrochemical exfoliation method. In typical electrochemical exfoliation method for synthesis of GQDs, sodium hydroxide is used for source of hydroxide (OH^-). The NaOH residue was still remained in GQDs solution after reaction. In the literature, calcium chloride ($CaCl_2$) was used to remove NaOH and make the white precipitate ($Ca(OH_2)$). However, the by-product (NaCl) still existed in the solution. Therefore, toluene post-treatment is a facile method for increasing the purity of GQD solution.

3.2 Chemical and Materials

Graphite rods (Sigma Aldrich, 99.9995 %), sodium hydroxide (Sigma Aldrich, ≥97%), ethanol (100%), toluene (Sigma Aldrich, 99.9%), PTFE syringe filter (0.22μm), cellulose dialysis membrane tubing (Fisher Scientific, 3,500 Da MWCO) were purchased for the synthesis of graphene quantum dots.

3.3 Apparatus and Equipment

UV-vis spectroscopy (Cary 60, Agilent Technologies) was used to investigate the UV-vis absorption spectra. Photoluminescence (PL) studies were done by fluorescence spectrofluorometer (QuantaMaster 400, HORIBA Scientific). The crystallinity of Graphite and GQDs was measured by X-ray diffraction (XRD, Empyrean Series 2, PANalytical). Raman spectroscopy (LabRam, Horiba) was employed to identify the existence and intensity ratio of D/G bands. Fourier-transform infrared spectrometer (FT-

IR, Nicolet iS10, ThermoFisher Scientific) and atomic force microscopy (AFM, Asylum Research MFP-3D) were utilized to know the functional groups and to determine the number of GQDs layers. Transmission electron microscope (TEM, Titan Themis 300) was used to determine particle size, distribution, and morphology of GQDs. Lastly, the electrochemical measurements were done by DC power supply (72-83500A, TENMA)

3.4 Preparation of GQDs

Graphite rods (diameter ~ 3 mm) were heated at 1050°C for 5 min in an open-air environment to make more defects and were naturally cooled at room temperature. And then, the rods were washed with DI water to eliminate the remaining particles from the surface of the graphite rods. Two individual graphite rods were used as the cathode and anode in the electrolyte (0.1 M NaOH in 49.75 ml ethanol and 0.25 ml water). The electrodes were immersed into the electrolyte for a few hours. After that, the electrochemical exfoliation process was done with the constant voltage of 20 V for 3 hr by DC power supply. The overall mechanism of GQDs synthesis is shown as Figure 3.2. The sodium salt of ethanol (C_2H_5ONa) and the hydroxide (OH^-) ions were produced by the reaction between NaOH and ethanol. The free OH^- ions induced the anode oxidation, which resulted in the electrochemical cutting of the graphite rod. After the completion of the reaction, the color of the solution was changed from colorless to yellow or red. The solution was centrifugated at 15,000 rpm for 20 min to remove the heavy particles. After taking the supernatant, the yellow supernatant was heated at 80°C to evaporate the ethanol. When the ethanol was almost evaporated, toluene was added to eliminate the

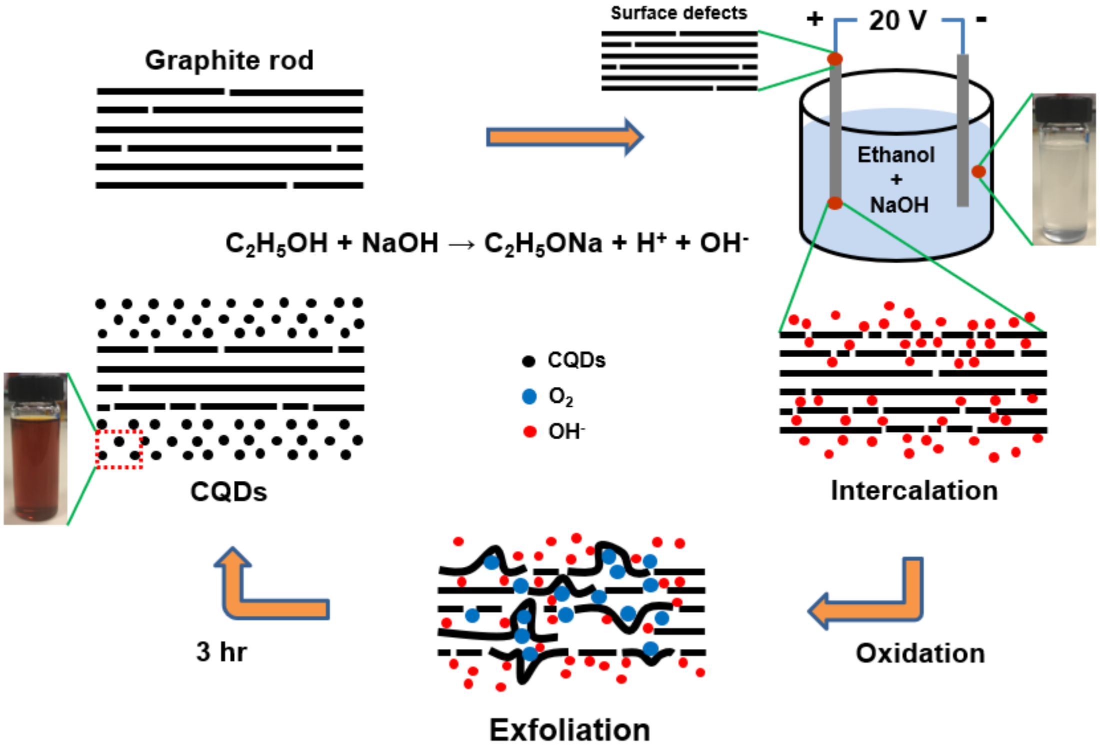

Figure 3.2 Diagram of electrochemical exfoliation of graphite rod

excessive NaOH. The toluene-based sample solution was centrifuged at 15000 rpm for 20 min. The toluene -based supernatant was mixed with DI water and then the water-based solution was collected by burette. Thereafter, the yellow solution was filtered using a syringe filter (0.22μm), and then the clear red solution was dialyzed through dialysis membrane (3,500 Da) for five days.

3.5 Result and Discussion

3.5.1 X-ray Diffraction (XRD)

As a starting material, graphite is a crystalline allotrope of carbon, which is composed of stacked graphene sheets, and is also one of the most readily available and inexpensive precursors.[35] The XRD patterns of graphite rod and synthesized GQDs are shown in Figure 3.3. The graphite rod has a significant peak at $2\theta = 26.4$ corresponding to the (002) plane with a d-spacing of 0.337 nm. The synthesized GQDs exhibit a broad diffraction peak at $2\theta = 25.3$ corresponding to the (002) plane with a d-spacing of 0.352 nm. The d-spacing was calculated by Bragg's equation as follows:

$$n \cdot \lambda = 2 \cdot d \cdot \sin(\theta)$$

where, n is the positive integer, λ is the wavelength of X-ray, d is the interplanar distance, and θ [rad] is the angle of the incident X-ray.[36] Compared to the d-spacing of graphite, the larger d-spacing of GQDs represents that the synthesized GQDs still have a lot of oxygen-rich functional groups. Based on the full width at half maximum (FWHM) value obtained from the diffraction peak, the average crystalline size of synthesized GQDs were estimated by Debye-Scherrer equation as follows:

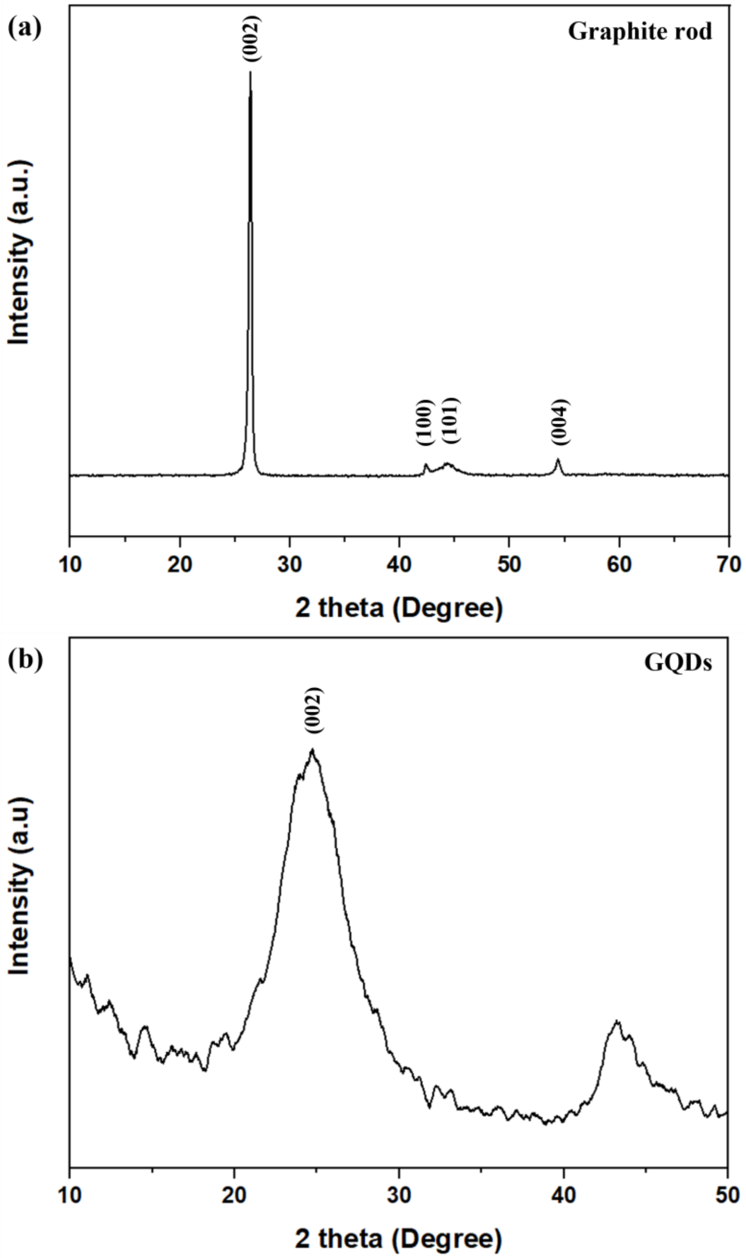

Figure 3.3 X-ray diffraction patterns of (a) graphite rod and (b) GQDs

$$D = K \cdot \lambda / \beta \cdot \cos(\theta)$$

Where, D is the crystalline size (nm), K is the Scherrer constant, λ is the wavelength of X-ray, θ is the diffraction angle, and β is the full width at half maximum (FWHM).[37] The estimated the average crystalline size of synthesized GQDs is 2.3 nm.

3.5.2 Raman Spectroscopy

Raman spectroscopy is one of the effective characterizations to find out the structural information of carbon-based materials.[38] In the Figure 3.4, two significant peaks of GQDs were observed, corresponding to D and G bands around 1350 cm^{-1} and 1580 cm^{-1}, respectively. The G band, corresponding to E_{2g} phonon at the Brillouin zone, comes from the presence of stretching C-C bonds in the sp^2 carbon network.[39] The G bands of graphite rod and GQDs are located at 1583 cm^{-1} and 1602 cm^{-1}. The D band indicates the presence of highly disordered carbon on the surface and edge of sp^3 carbon or functional groups. The D bands of graphite and GQDs are positioned at 1355 cm^{-1} and 1351 cm^{-1}. The increase in sp^3-hybridized carbon or functional groups combining with sp3-hybridized carbon causes the D band to broaden.[40] The degree of disorder can be measured from the intensity ratio of the D band to the G band (I_D/I_G). The I_D/I_G of graphite and GQDs are 0.28 and 0.95, respectively. The increase in I_D/I_G of GQDs represents that the number of defects in GQDs increases compared to graphite rod through the electrochemical exfoliation process.

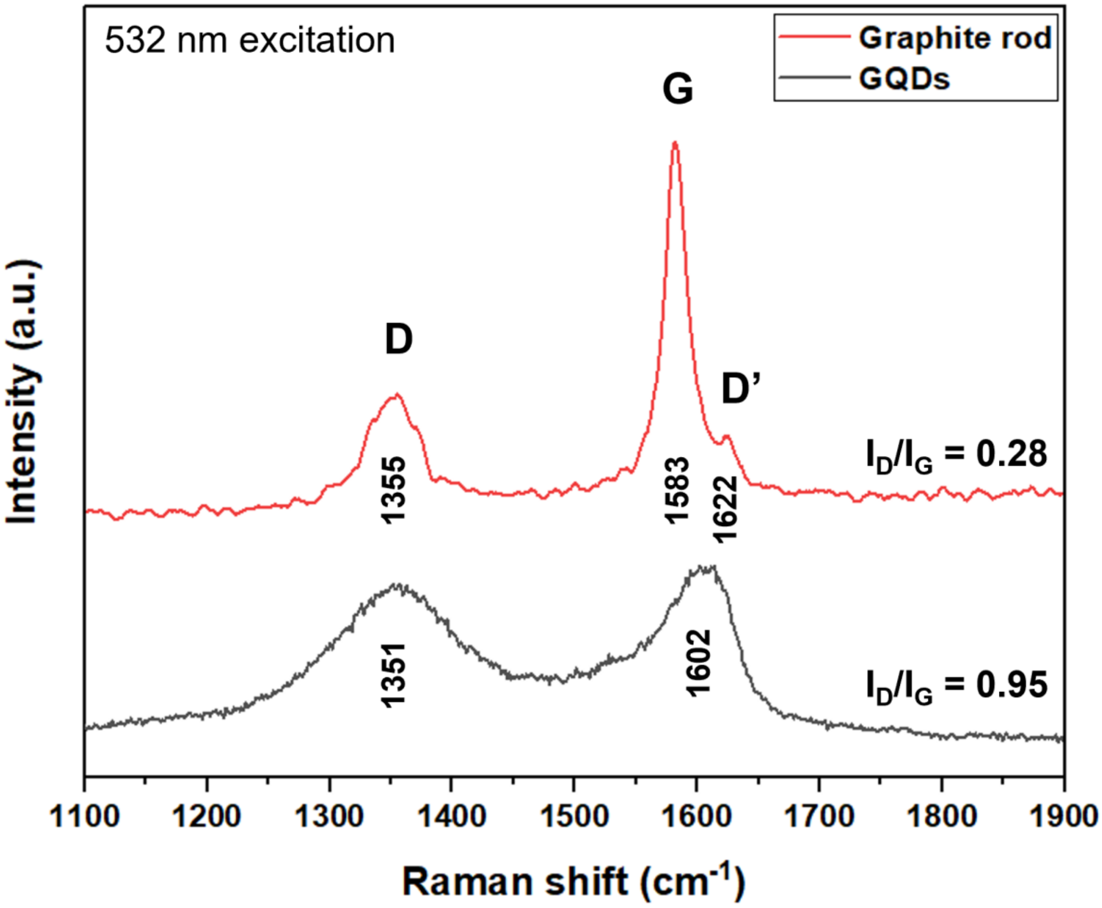

Figure 3.4 Raman spectra of graphite rod and GQDs measured with 532 nm laser

3.5.3 Fourier-transform Infrared Spectroscopy (FT-IR)

Fourier transform infrared spectroscopy (FT-IR) was used to investigate the functional groups of graphite rod and synthesized GQDs as shown in Figure 3.5. While graphite rod has no significant peaks observed, the FT-IR spectra of GQDs indicated the presence of hydroxyl groups (at 3386 cm^{-1} and 3054 cm^{-1}), and C-O groups (at 1087 cm^{-1} and 1025 cm^{-1}). As one of the key features, the solubility of GQDs in water is determined by these hydroxyl and carboxyl groups. The absorption spectra at 1465 cm^{-1}, 879 cm^{-1}, and 748 cm^{-1} corresponds to C-H groups. The small peaks at 1087 cm^{-1} and 1025 cm^{-1} were attributed to the C-O stretching. In addition, the absorption peaks included 1712 cm^{-1} for carbonyl C=O stretching and 1627 cm^{-1} for aromatic rings C=C groups. These spectra implied that GQDs were completed oxidized from graphite rod through the electrochemical exfoliation method.

3.5.4 UV-Visible Spectroscopy and Fluorescence

In order to examine the absorbance and fluorescence properties of the resulting GQDs, it is necessary first to understand their chemical origin and surface states. Spectroscopic analysis of UV-visible and photoluminescence (PL) provide information on the optical characteristics of these GQDs.[41] Figure 3.6 shows the UV-Visible spectrum of GQDs prepared using sodium hydroxide as a reducing agent in mixed water and ethanol medium. Two prominent absorption peaks at 227 nm and 358 nm were observed. The peak observed at 227 nm corresponds to aromatic π-π^* transitions of sp^2 C=C bonds.[11] The peak at 358 nm results from n- π^* transition of C=O bonds or other

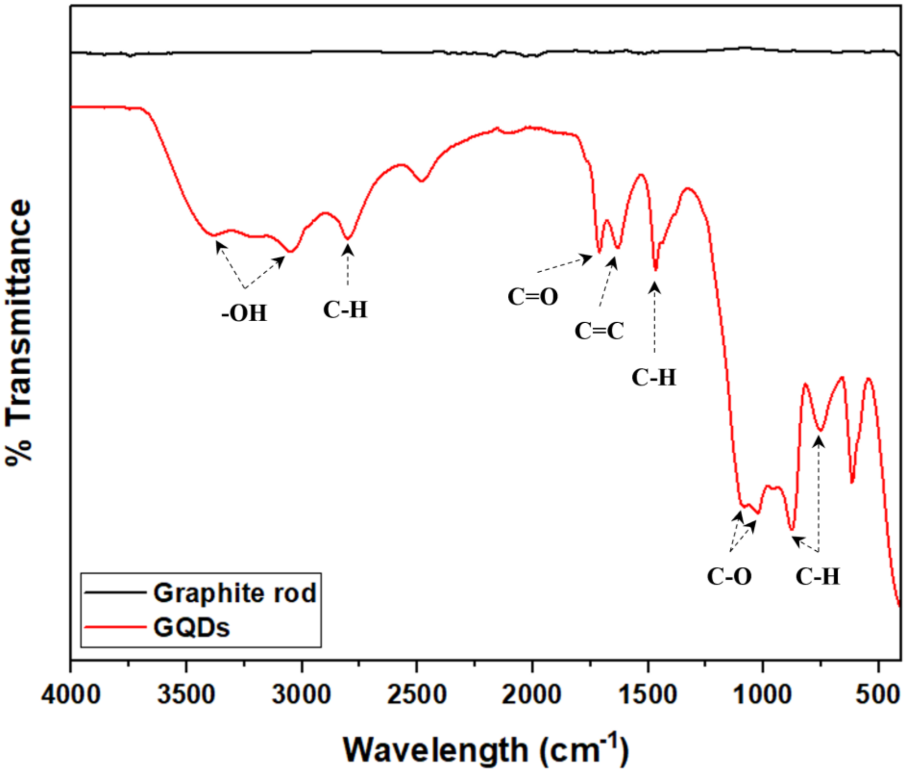

Figure 3.5 FTIR spectra of graphite rod and GQDs

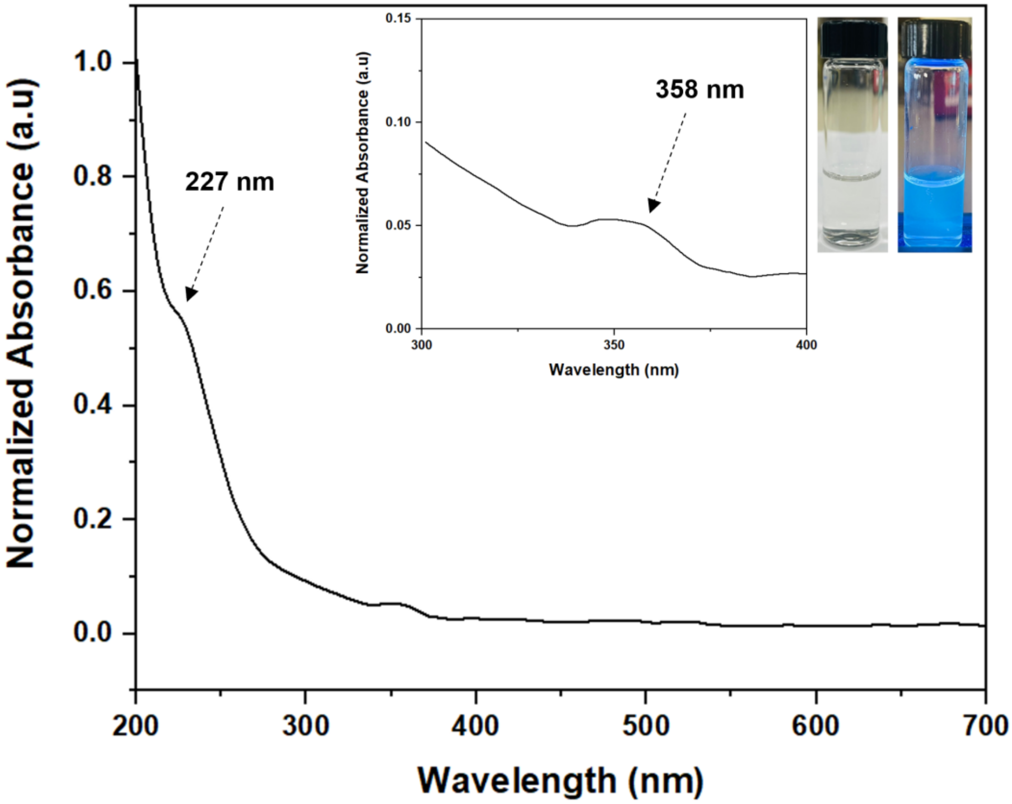

Figure 3.6 UV-Visible absorption spectra of GQDs and their images under visible light and 365 nm wavelength

functional groups on the surface of GQDs.[42] The images of GQDs solution obtained under normal visible light and upon UV light illumination at a fixed wavelength of 365 nm show their blue emission color.

The PL spectra are also used to explore the fluorescence properties of GQDs and are shown in Figure 3.7. The emission of GQDs were investigated at various excitation wavelengths from 300 nm to 340 nm. In Figure 3.7, the fluorescence spectra of GQDs excited at a fixed wavelength of 320 nm. The highest intensity of emission occurs at 424 nm for GQDs upon excitation at 320 nm. In order to double check the emission and excitation wavelengths of GQDs, the excitation of GQDs was examined at multiple emission wavelengths ranging from 400 nm to 450 nm. As a result, the maximum intensities of excitation and emission peaks occur at 320 nm and 424 nm, respectively.

3.5.5 Transmission Electron Microscopy (TEM)

Transmission electron microscopy (TEM) is used to investigate the structural morphology and particle size of GQDs as shown in Figure 3.8. It also shows that the as-synthesized GQDs possess a nearly spherical shape. The particle size distribution graph is shown in Figure 3.9 (b). The average particle size of GQDs is estimated to be 11.4 nm, as determined by statistical analysis of particles using ImageJ software.

3.5.6 Atomic Force Microscopy (AFM)

Atomic Force Microscopy (AFM) is an effective technique to estimate the

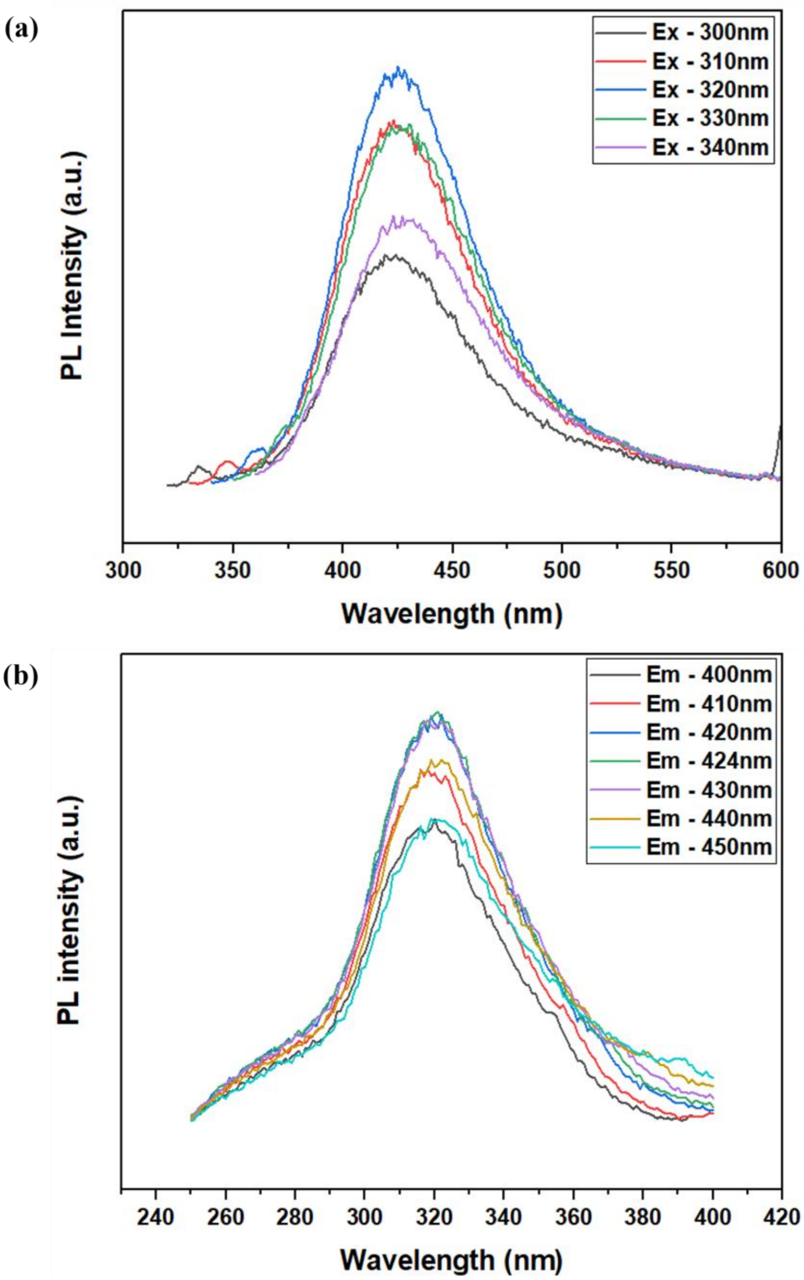

Figure 3.7 (a) PL emission of GQDs at different excitation wavelengths (b) PL excitation of GQDs at different emission wavelengths

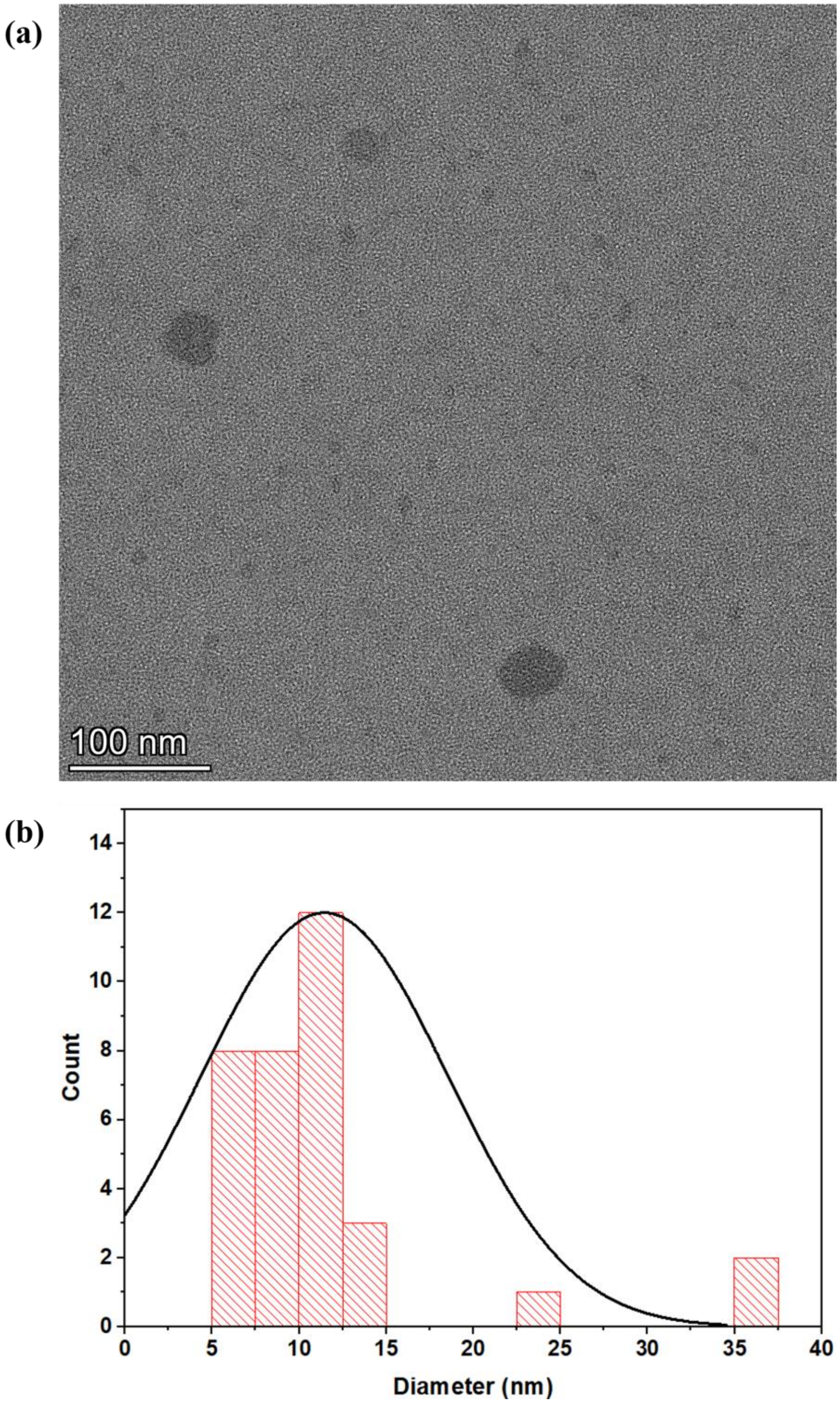

Figure 3.8 TEM image and size distribution of the synthesized GQDs

number of layers of GQDs. Silicon wafer substrate was used for the preparation of AFM sample. The AFM sample was prepared using a spin coater (at 2000 rpm for 30 sec). The AFM image shows that GQDs particles are well-dispersed and have a few layers, as shown in Figure 3.9. From the height profile of GQDs, the average height obtained was around 1.19 nm. It means that the number of layers is less than four graphene layers because the thickness of monolayer graphene is being considered around 0.345 nm. The topography image of GQDs in Figure 3.10 (c) came from the height profile along the line in the image.

3.6 Conclusions

In summary, I have successfully synthesized GQDs by electrochemical exfoliation method using graphite rods as both anode and cathode in NaOH/ethanol solution. Heat treatment of graphite rods at high temperature result in the increase in the defect sites on the surface of graphite rods. The optical properties of synthesized GQDs were investigated by UV-visible spectroscopy and fluorescence spectroscopy. The particle size, crystalline structure, functional groups, topography, and structural information of GQDs were analyzed by TEM, XRD, FT-IR, AFM, and Raman, respectively. The GQDs have average size of 11.4 nm and exhibit blue color under 365 nm UV irradiation. This simple synthesis method and their optical, electronic, structural properties make them a good candidate for many advanced applications such as catalyst, bioimaging, sensors, solar-cell, drug delivery, supercapacitors, and batteries. In Chapter 4, the new type of photo-rechargeable battery and its performance improvement using

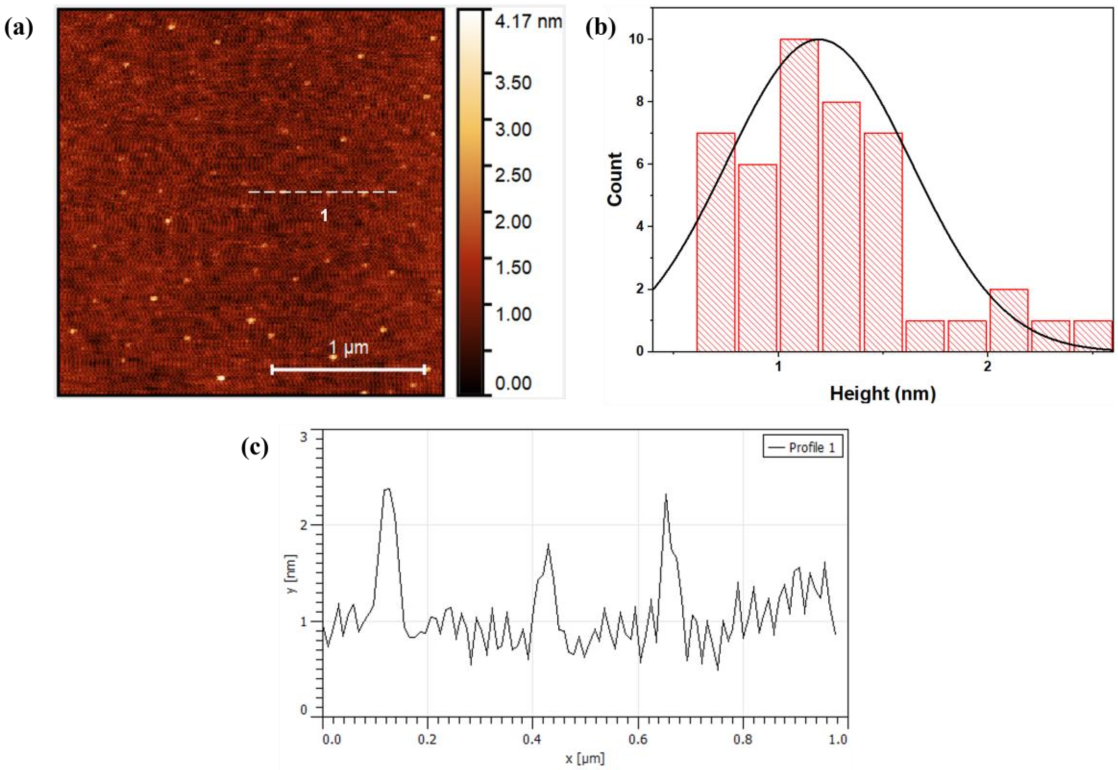

Figure 3.9 (a) AFM image, (b) height profile, and (c) surface roughness of GQDs

GQDs will be further discussed.

Reference

1. Elvati, P.; Baumeister, E.; Violi, A. J. R. a., Graphene quantum dots: effect of size, composition and curvature on their assembly. **2017,** *7* (29), 17704-17710.

2. https://www.newworldencyclopedia.org/entry/Graphite.

3. Kharisov, B. I.; Kharissova, O. V., *Carbon allotropes: metal-complex chemistry, properties and applications*. Springer: 2019.

4. Androulidakis, C.; Koukaras, E. N.; Frank, O.; Tsoukleri, G.; Sfyris, D.; Parthenios, J.; Pugno, N.; Papagelis, K.; Novoselov, K. S.; Galiotis, C. J. S. R., Failure processes in embedded monolayer graphene under axial compression. **2014,** *4* (1), 1-8.

5. Kwon, W.; Rhee, S.-W. J. C. c., Facile synthesis of graphitic carbon quantum dots with size tunability and uniformity using reverse micelles. **2012,** *48* (43), 5256-5258.

6. Cahay, M. In *Quantum confinement VI: nanostructured materials and devices: proceedings of the international symposium*, The Electrochemical Society: 2001.

7. Ponomarenko, L. A.; Schedin, F.; Katsnelson, M. I.; Yang, R.; Hill, E. W.; Novoselov, K. S.; Geim, A. K. J. S., Chaotic Dirac billiard in graphene quantum dots. **2008**.

8. Paulo, S.; Palomares, E.; Martinez-Ferrero, E. J. N., Graphene and carbon quantum dot-based materials in photovoltaic devices: from synthesis to applications. **2016,** *6* (9), 157.

9. Li, Y.; Shu, H.; Wang, S.; Wang, J. J. T. J. o. P. C. C., Electronic and optical properties of graphene quantum dots: the role of many-body effects. **2015,** *119* (9), 4983-4989.

10. Son, J.; Lee, S.; Kim, S. J.; Park, B. C.; Lee, H.-K.; Kim, S.; Kim, J. H.; Hong, B. H.; Hong, J. J. N. c., Hydrogenated monolayer graphene with reversible and tunable wide band gap and its field-effect transistor. **2016,** *7* (1), 1-7.

11. Eda, G.; Lin, Y. Y.; Mattevi, C.; Yamaguchi, H.; Chen, H. A.; Chen, I. S.; Chen, C. W.; Chhowalla, M. J. A. m., Blue photoluminescence from chemically derived graphene oxide. **2010,** *22* (4), 505-509.

12. Ozfidan, I.; Korkusinski, M.; Hawrylak, P. J. p. s. s. R. R. L., Electronic properties and electron–electron interactions in graphene quantum dots. **2016,** *10* (1), 13-23.

13. Nakada, K.; Fujita, M.; Dresselhaus, G.; Dresselhaus, M. S. J. P. R. B., Edge state in graphene ribbons: Nanometer size effect and edge shape dependence. **1996,** *54* (24), 17954.

14. Ezawa, M. J. P. E. L.-d. S.; Nanostructures, Graphene nanoribbon and graphene nanodisk. **2008,** *40* (5), 1421-1423.

15. Huang, Z.; Qu, J.; Peng, X.; Liu, W.; Zhang, K.; Wei, X.; Zhong, J. J. p. s. s. R. R. L., Quantum confinement in graphene quantum dots. **2014,** *8* (5), 436-440.

16. Cui, L.; Ren, X.; Sun, M.; Liu, H.; Xia, L. J. N., Carbon Dots: Synthesis, Properties and Applications. **2021,** *11* (12), 3419.

17. Hai, X.; Feng, J.; Chen, X.; Wang, J. J. J. o. M. C. B., Tuning the optical properties of graphene quantum dots for biosensing and bioimaging. **2018,** *6* (20), 3219-3234.

18. Perini, G.; Palmieri, V.; Ciasca, G.; De Spirito, M.; Papi, M. J. I. j. o. m. s., Unravelling the potential of graphene quantum dots in biomedicine and neuroscience. **2020,** *21* (10), 3712.

19. Zhu, Z.; Ma, J.; Wang, Z.; Mu, C.; Fan, Z.; Du, L.; Bai, Y.; Fan, L.; Yan, H.; Phillips, D. L. J. J. o. t. A. C. S., Efficiency enhancement of perovskite solar cells through fast electron extraction: the role of graphene quantum dots. **2014,** *136* (10), 3760-3763.

20. Zhang, S.; Sui, L.; Dong, H.; He, W.; Dong, L.; Yu, L. J. A. a. m.; interfaces, High-performance supercapacitor of graphene quantum dots with uniform sizes. **2018,** *10* (15), 12983-12991.

21. Zhao, C.; Song, X.; Liu, Y.; Fu, Y.; Ye, L.; Wang, N.; Wang, F.; Li, L.; Mohammadniaei, M.; Zhang, M. J. J. o. N., Synthesis of graphene quantum dots and their applications in drug delivery. **2020,** *18* (1), 1-32.

22. Lu, Q.; Zhang, Y.; Liu, S. J. J. o. M. C. A., Graphene quantum dots enhanced photocatalytic activity of zinc porphyrin toward the degradation of methylene blue under visible-light irradiation. **2015,** *3* (16), 8552-8558.

23. Facure, M. H.; Schneider, R.; Mercante, L. A.; Correa, D. S. J. E. S. N., A review on graphene quantum dots and their nanocomposites: from laboratory synthesis towards agricultural and environmental applications. **2020,** *7* (12), 3710-3734.

24. De, B.; Karak, N. J. J. o. M. C. A., Recent progress in carbon dot–metal based nanohybrids for photochemical and electrochemical applications. **2017,** *5* (5), 1826-1859.

25. Shen, J.; Zhu, Y.; Yang, X.; Li, C. J. C. c., Graphene quantum dots: emergent nanolights for bioimaging, sensors, catalysis and photovoltaic devices. **2012,** *48* (31), 3686-3699.

26. Zhao, P.; Yang, M.; Fan, W.; Wang, X.; Tang, F.; Yang, C.; Dou, X.; Li, S.; Wang, Y.; Cao, Y. J. P.; Characterization, P. S., Facile One-Pot Conversion of Petroleum Asphaltene to High Quality Green Fluorescent Graphene Quantum Dots and Their Application in Cell Imaging. **2016,** *33* (9), 635-644.

27. Ahirwar, S.; Mallick, S.; Bahadur, D. J. A. o., Electrochemical method to prepare graphene quantum dots and graphene oxide quantum dots. **2017,** *2* (11), 8343-8353.

28. Yoon, H.; Chang, Y. H.; Song, S. H.; Lee, E. S.; Jin, S. H.; Park, C.; Lee, J.; Kim, B. H.; Kang, H. J.; Kim, Y. H. J. A. M., Intrinsic photoluminescence emission from subdomained graphene quantum dots. **2016,** *28* (26), 5255-5261.

29. Hu, S.-L.; Niu, K.-Y.; Sun, J.; Yang, J.; Zhao, N.-Q.; Du, X.-W. J. J. o. M. C., One-step synthesis of fluorescent carbon nanoparticles by laser irradiation. **2009,** *19* (4), 484-488.

30. Ren, Q.; Ga, L.; Ai, J. J. A. o., Rapid synthesis of highly fluorescent nitrogen-doped graphene quantum dots for effective detection of ferric ions and as fluorescent ink. **2019,** *4* (14), 15842-15848.

31. Pan, D.; Zhang, J.; Li, Z.; Wu, M. J. A. m., Hydrothermal route for cutting graphene sheets into blue-luminescent graphene quantum dots. **2010,** *22* (6), 734-738.

32. Tian, R.; Zhong, S.; Wu, J.; Jiang, W.; Shen, Y.; Wang, T. J. O. M., Solvothermal method to prepare graphene quantum dots by hydrogen peroxide. **2016,** *60*, 204-208.

33. Ma, C.-B.; Zhu, Z.-T.; Wang, H.-X.; Huang, X.; Zhang, X.; Qi, X.; Zhang, H.-L.; Zhu, Y.; Deng, X.; Peng, Y. J. N., A general solid-state synthesis of chemically-doped fluorescent graphene quantum dots for bioimaging and optoelectronic applications. **2015,** *7* (22), 10162-10169.

34. Ding, X. J. J. o. M. C. C., Direct synthesis of graphene quantum dots on hexagonal boron nitride substrate. **2014,** *2* (19), 3717-3722.

35. Tan, X.; Li, Y.; Li, X.; Zhou, S.; Fan, L.; Yang, S. J. C. C., Electrochemical synthesis of small-sized red fluorescent graphene quantum dots as a bioimaging platform. **2015,** *51* (13), 2544-2546.

36. Pope, C. G. J. J. o. c. e., X-ray diffraction and the Bragg equation. **1997,** *74* (1), 129.

37. Kumar, S.; Layek, S.; Yashpal, M.; Ojha, A. K. J. J. o. M.; Materials, M., Room temperature ferromagnetism in undoped and Mn doped CdO nanostructures. **2015,** *393*, 555-561.

38. Ferrari, A. C.; Robertson, J. J. P. r. B., Interpretation of Raman spectra of disordered and amorphous carbon. **2000,** *61* (20), 14095.

39. Tuinstra, F.; Koenig, J. L. J. T. J. o. c. p., Raman spectrum of graphite. **1970,** *53* (3), 1126-1130.

40. Kudin, K. N.; Ozbas, B.; Schniepp, H. C.; Prud'Homme, R. K.; Aksay, I. A.; Car, R. J. N. l., Raman spectra of graphite oxide and functionalized graphene sheets. **2008,** *8* (1), 36-41.

41. Muthurasu, A.; Dhandapani, P.; Ganesh, V. J. N. J. o. C., Facile and simultaneous synthesis of graphene quantum dots and reduced graphene oxide for bio-imaging and supercapacitor applications. **2016,** *40* (11), 9111-9124.

42. Lin, L.; Zhang, S. J. C. c., Creating high yield water soluble luminescent graphene quantum dots via exfoliating and disintegrating carbon nanotubes and graphite flakes. **2012,** *48* (82), 10177-10179.

Chapter 4. Engineering Graphene Quantum Dots: Application for Photo-rechargeable Battery

4.1 Introduction

Titanium dioxide (TiO_2) is extensively utilized as a good photoelectrode candidate due to its low toxicity, reasonable price, and good photostability. Especially, TiO_2 has a conduction band that is situated below the lowest unoccupied molecular orbital (LUMO) of the dye to promote the effective electron transmission, However, TiO_2 has some disadvantages, such as large bandgap (3.0 eV for rutile and 3.2 eV for anatase), poor light absorption on visible region, poor conductivity, high carrier recombination, and lack of charge-carrier transport.[1-3] The use of GQDs for photoelectrode was reported that they can improve the light absorption to visible region, decrease the TiO_2 bandgap, and improve the charge transfer and efficiency by employing the graphene-based materials in the dye-sensitized solar cell (DSSC).[4-6] But research on the use of GQDs and N719 dye in the photo-rechargeable battery has not been reported yet. The objective of this research is to investigate the effect of use of GQDs and N719 dye in our photo-rechargeable battery, resulting in the performance improvement of the photo-rechargeable battery.

4.2 Chemical and Materials

Di-tetrabutylammonium cis-bis(isothiocyanato)bis(2,2′-bipyridyl-4,4′-dicarboxylato)ruthenium(II) (N719, Sigma Aldrich, 95%), FTO (Fluorine-doped Tin

Oxide) glass (surface resistivity ~ 13Ω/sq, Sigma Aldrich), titania paste (Sigma Aldrich), lithium iron phosphate (LFP, MTI corporation), conductive carbon black (super P, MTI corporation), propylene carbonate (PC, Sigma Aldrich, 99.7%), lithium bis-trifluoromethanesulfonimide (LiTFSi, Sigma Aldrich), 1-methyl-2-pyrrolidinone (NMP, Fisher Scientific, 99%), polyvinylidene fluoride (PVDF, Sigma Aldrich, Mw ~ 534,000 $g \cdot cm^{-1}$), chloroplatinic acid hexahydrate (Sigma Aldrich), lithium iodide (LiI, Sigma Aldrich), Iodine (I_2, Sigma Aldrich, 99.8%), 4-tert-Butylpyridine (Sigma Aldrich, 98%), guanidine thiocyanate (Sigma Aldrich, 99%), valeronitrile (Sigma Aldrich, 99.5%), acetonitrile (Sigma Aldrich, 99.8%), surlyn film (Solaronix, 60μm thickness), epoxy glue, were purchased for the fabrication of photo-rechargeable battery

4.3 Apparatus and Equipment

UV-vis spectroscopy (Cary 5000, Agilent Technologies) was used to investigate the UV-vis absorption spectra. The crystallinity structure was measured by X-ray diffraction (XRD, Empyrean Series 2, PANalytical). Raman spectroscopy (LabRam, Horiba) was employed to identify the existence of D/G bands. Fourier-transform infrared spectrometer (FT-IR, Nicolet iS10, ThermoFisher Scientific) was used to investigate the functional groups. The electrochemical measurements such as LSV, chronoamperometry, electrochemical impedance spectroscopy (EIS), and charge/discharge test were done by potentiostat/galvanostat (VersaSTAT 4, AMETEK). A solar simulator (Newport, Oriel Sol3A Class AAA Solar Simulator, 450 W Xenon) was used for the light source (AM 1.5G, $100mW \cdot cm^{-2}$).

4.4 Experimental Procedure

The overall procedure of the cell preparation, including electrodes and electrolytes, is already mentioned in Chapter 3.4. The synthesized TiO_2 electrode is soaked into the pre-synthesized GQDs solution (1mg/ml) and the prepared N719 dye solution for 96 h and 24 h, respectively. The N719 dye solution is composed of 0.5 mM Di-tetrabutylammonium cis-bis(isothiocyanato)bis(2,2′-bipyridyl-4,4′-dicarboxylato)ruthenium(II) (Sigma Aldrich, 95%) in ethanol. After a certain soaking time, the sensitized electrodes are washed three times with DI water to remove the residue on the surface of the electrodes. And then, the electrodes are dried by a nitrogen spray gun and heated on the hotplate at 100°C overnight.

4.5 Result and Discussion

4.5.1 UV-visible Spectroscopy

The optical properties of TiO_2, GQDs/TiO_2, N719/TiO_2, and N719/GQDs/TiO_2 were investigated by UV-visible spectroscopy, as shown in Figure 4.1 (a). In the UV-visible graph, the intensity of the absorbance peak is determined by the thickness of each deposited sample on the substrate. The UV-visible spectra of all samples show a broad absorbance peak in the UV region (below 400nm). There is not quite an absorbance difference between TiO_2 and GQDs/TiO_2. In addition, a significant peak observed of N719/TiO_2 and N719/GQDs/TiO_2 samples are identified at 501 nm and 538 nm, respectively. Both N719/TiO_2 and N719/GQDs/TiO_2 electrodes were soaked into the dye solution for 24 h. Based on Figure 4.1 (b), N719/GQDs/TiO_2 electrode absorbs more

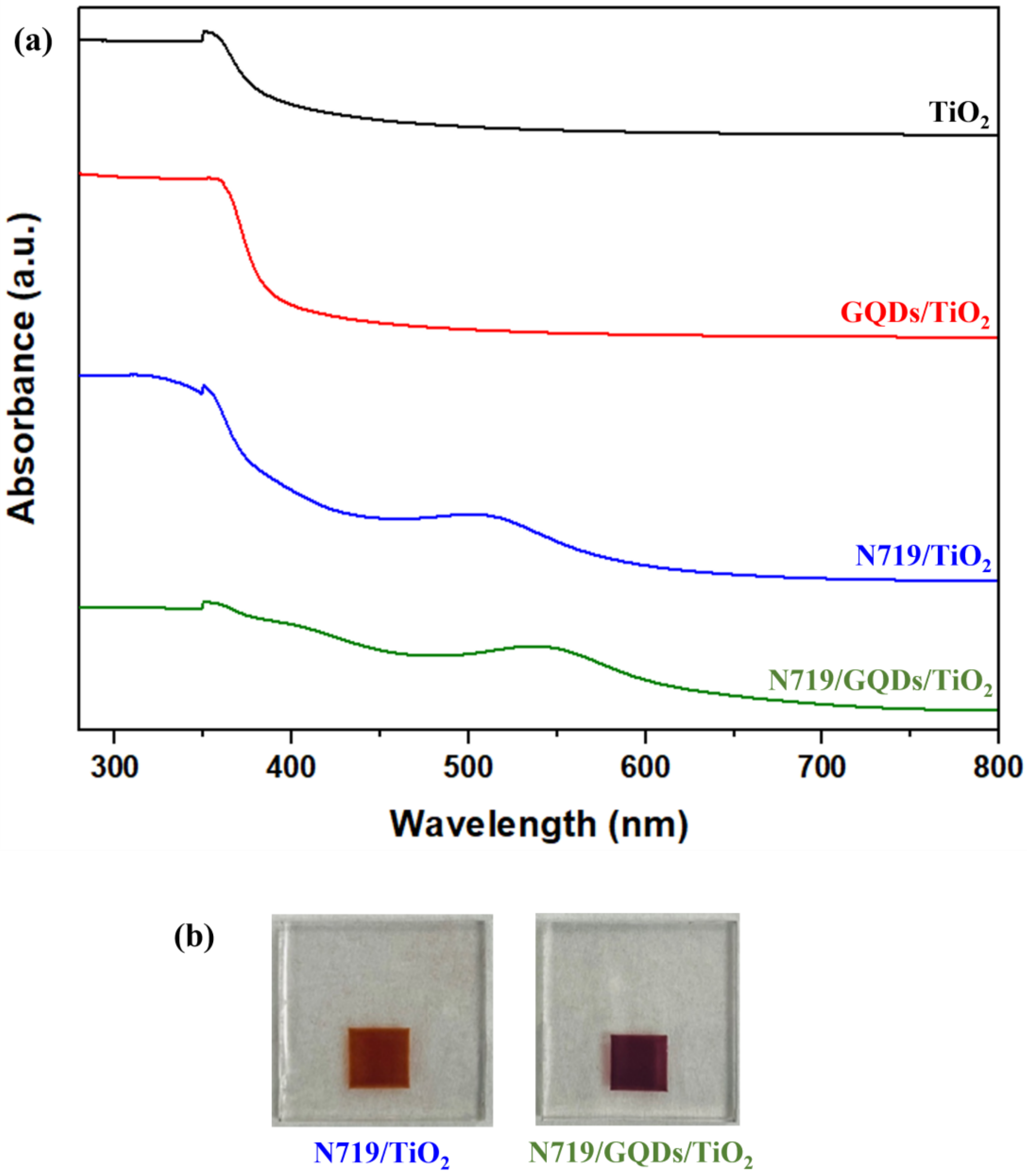

Figure 4.1 (a) UV-visible spectra of TiO_2, GQDs/TiO_2, N719/TiO_2, and N719/GQDs/TiO_2, (b) Images of N719/TiO_2 and N719/GQDs/TiO_2 electrodes

N719 dye. This results in the absorbance peak shift from 501 nm to 538 nm. The color difference between the two electrodes may cause the hydrophilic functional group (hydroxyl and carboxyl groups) of GQDs. The N719 dye is immersed in ethanol, which has a hydrophilic functional group. So, the GQDs and ethanol act as a bridge between TiO_2 and N719.

4.5.2 X-ray Diffraction

The crystal structure and growth direction of the synthesized TiO_2 paste, GQDs/TiO_2, and N719/GQDs/TiO_2 on FTO glass substrate were investigated by the XRD patterns as shown in Figure 4.2. The characteristics diffraction peak of the commercial TiO_2 paste indicates the anatase TiO_2 phase. The peaks observed at 25.32°, 37.02°, 37.96°, 47.96°, 54.08°, 55.04°, 62.84°, 69.06°, 70.18°, and 75.18° are corresponding to (101), (103), (004), (200), (105), (211), (204), (116), (220), and (215) lattice plane of anatase TiO_2. There are no peaks observed located around 36.1°, 41.2°, and 56.7°, indicating (004), (110), and (114) planes of rutile TiO_2. There are no significant peak differences between GQDs/TiO_2 and N719/GQDs/TiO_2 compared with pristine TiO_2. This can be owing to low quantity and poor intensity of GQDs.[7] In Figure 2.4.1, the diffraction peak of GQDs located at 25.3° corresponds to graphite's (002) plane. This peak from GQDs can be overlapped with the (101) plane of TiO_2, which is located at 25.32°. In addition, this may also indicate that GQDs and N719 did not affect the crystal structure of TiO_2.[8]

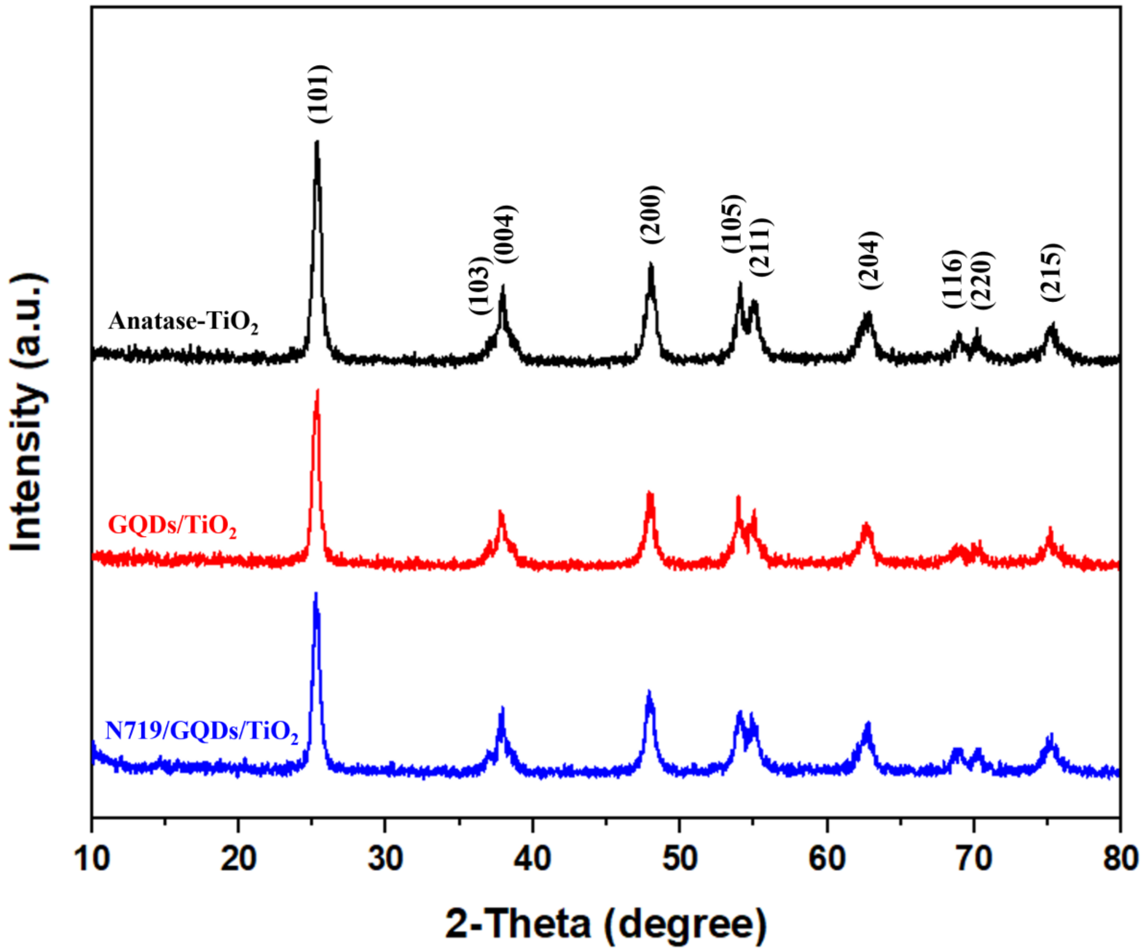

Figure 4.2 XRD patterns of the TiO_2, $GQDs/TiO_2$, and $N719/GQDs/TiO_2$

4.5.3 Raman and FT-IR Spectroscopy

Both Raman and FT-IR spectroscopy give precise information on chemical structure, phase, and molecular interactions. The production of the TiO_2 anatase phase and the presence of GQDs in GQDs/TiO_2 nanocomposites are identified by Raman analysis. Furthermore, it is a significant tool for determining the structure of graphene-based materials based on the quality and quantity of graphene layers and the type of defects and disorder. The Raman spectra of synthesized TiO_2, GQDs/TiO_2, N719/TiO_2, N719/GQDs/TiO_2 are shown in Figure 4.3. The characteristic peaks of pristine TiO_2 are located at 396, 516, and 638 cm^{-1}, corresponding to the B_{1g}, A_{1g} + B_{1g}, and E_g mode vibration of the anatase TiO_2 phase.[9] In the spectrum of GQDs/TiO_2, two additional peaks for GQDs are identified at 1356 and 1605 cm^{-1}, respectively, which can be attributed to disordered sp^2 carbon (D-band) and well-ordered graphite (G-band). The significant peaks of N719/GQDs/TiO_2 are observed including the peaks from TiO_2, N719, and GQDs. In particular, the D band of N719/GQDs/TiO_2 electrode are identified at 1353 cm^{-1}. However, The G band of N719/GQDs/TiO_2 electrode are overlapped with the peak (at 1608 cm^{-1}) from the N719. The presence of GQDs from both GQDs/TiO_2 and N719/GQDs/TiO_2 electrodes is confirmed by Raman analysis.

FT-IR analysis of TiO_2, GQDs/TiO_2, N719/TiO_2, N719/GQDs/TiO_2 were also conducted to identify the functional groups as shown in Figure 4.4. The GQDs have a lot of oxygen containing functional groups. However, there are no peak differences between TiO_2 and GQDs/TiO_2. This may cause the lack of quantity of GQDs in the GQDs/ TiO2 electrode.

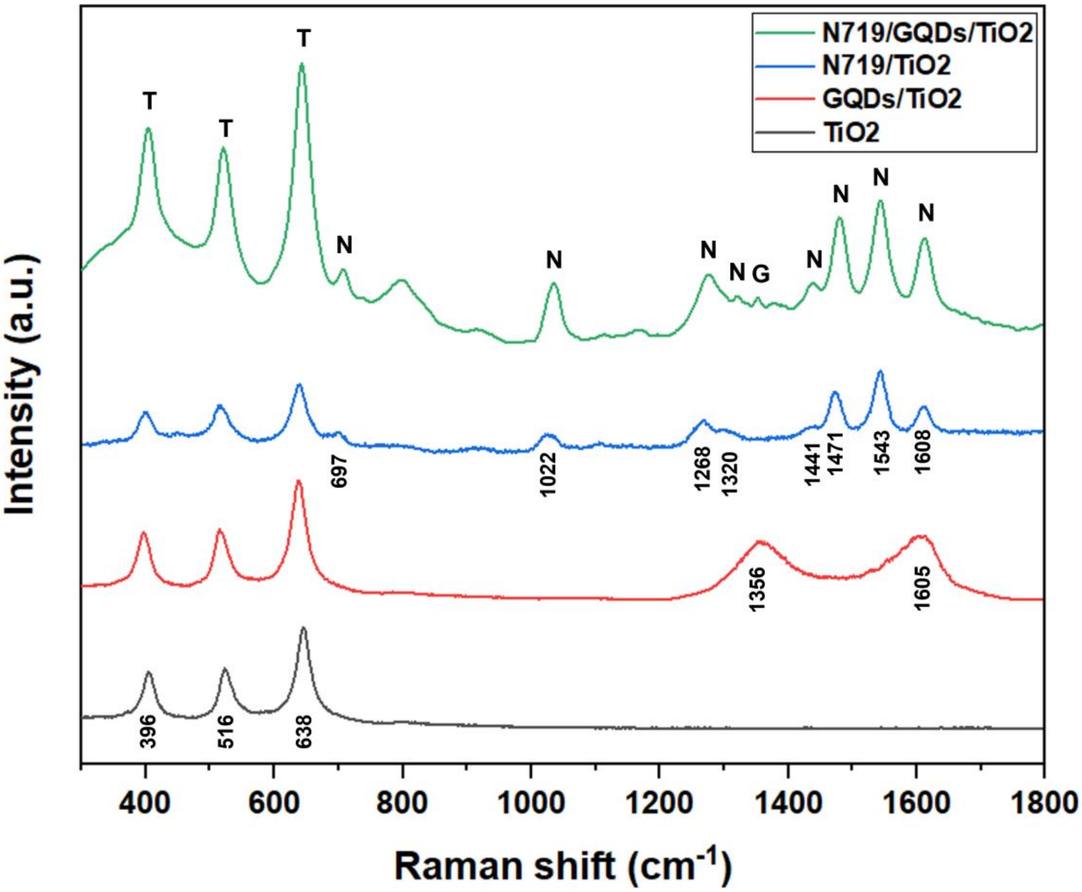

Figure 4.3 Raman spectra of the TiO_2, GQDs/TiO_2, N719/TiO_2, and N719/GQDs/TiO_2 with 532 nm laser excitation

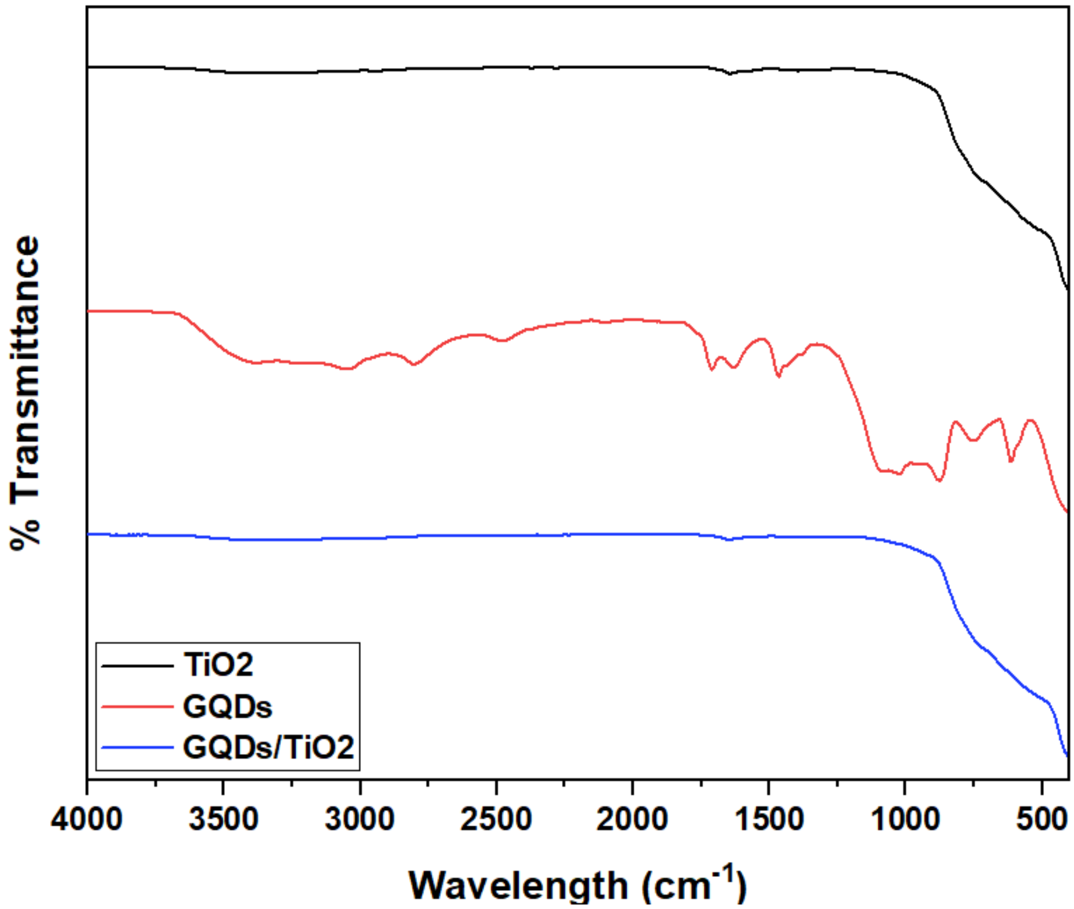

Figure 4.4 FT-IR spectra of the TiO_2, GQDs, and GQDs/TiO_2

4.5.4 Scanning Electron Microscopy (SEM) and Energy Dispersive X-ray Analysis (EDX)

Figure 4.5 shows the SEM image (a) and EDX analysis (b) of the GQDs/TiO_2 electrode. The EDX graph represents the existence of chemical elements in the GQDs/TiO2. The highest peak is titanium (Ti), which accounts for 54.9 wt%. The second highest peak is oxygen. The other chemical elements such as carbon (C), sodium (Na), calcium (Ca) exist in the GQDs/TiO_2. The portions of Na and Ca are negligible, and carbon indicates the presence of GQDs in the sample. 2.7 wt% of GQDs exists in the GQDs/TiO_2 electrodes.

4.5.5 Electrochemical Analysis

In order to confirm the characteristics of TiO_2, GQDs/TiO_2, N719/TiO_2, N719/GQDs/TiO_2, the electrochemical analysis, such as LSV, chronoamperometry, EIS, and charge/discharge tests are used. The electrode containing 50 mM chloroplatinic acid hexahydrate are used with iodine-based electrolyte for only LSV, chronoamperometry, and EIS tests. In Figure 4.6, LSV measurements are carried out with 0.005 V/s scan rate, ranging from -1 V to 1V. So as to calculate the photovoltaic efficiency of the solar battery, the values of Voc, Jsc, P_{in}, and FF are obtained, as shown in Table 4.1. With the use of GQDs, higher conversion efficiency (0.169% and 2.784%) is confirmed by using GQDs/TiO_2 and N719/GQDs/TiO_2 electrodes in the solar battery compared to TiO_2 (0.133%). Especially, the photocurrent densities of the GQDs/TiO_2 and N719/GQDs/TiO_2 electrodes also have 1.2 and 19 times higher than pristine TiO_2

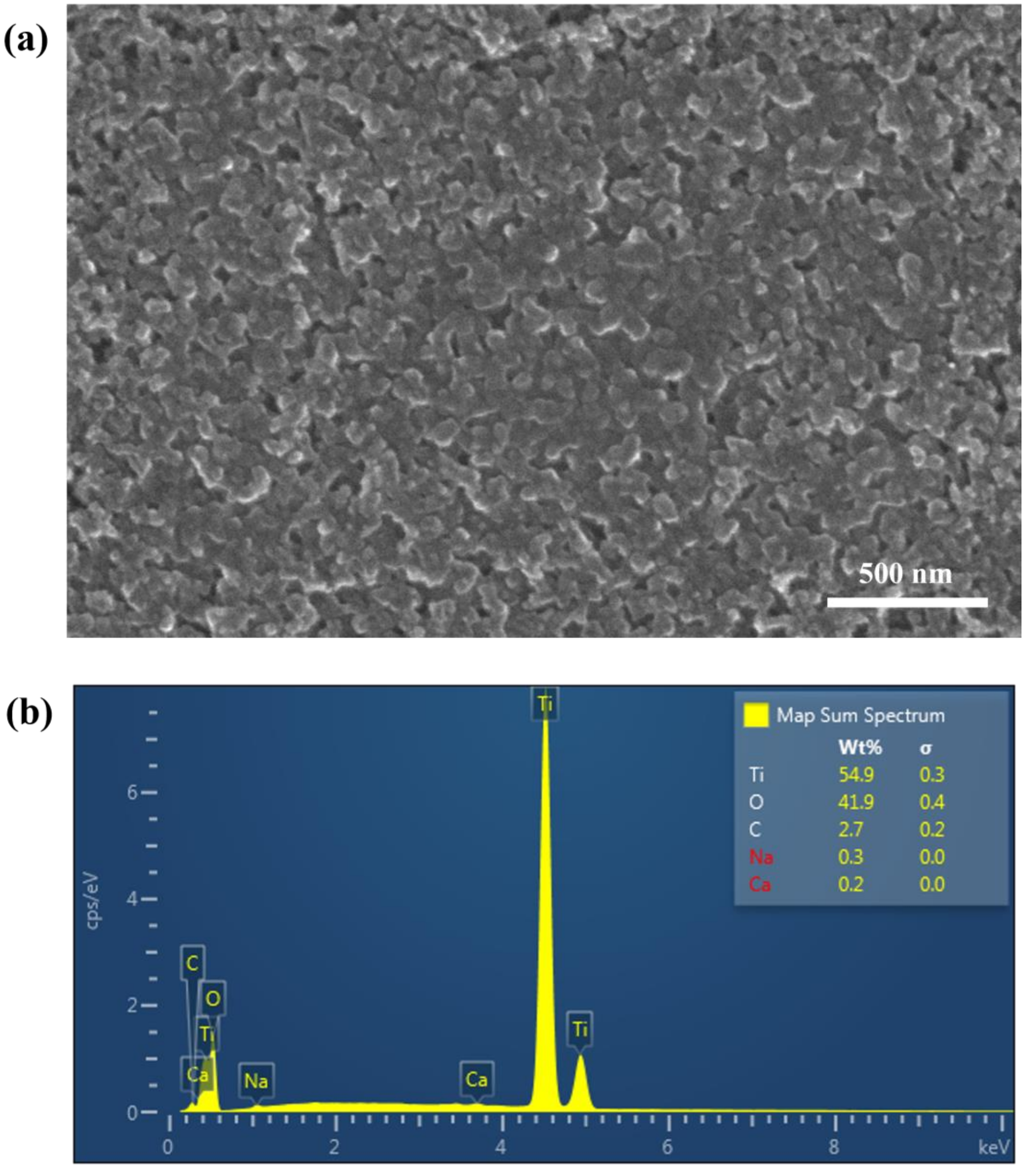

Figure 4.5 (a) SEM image and (b) EDX analysis of GQD/TiO_2 electrode

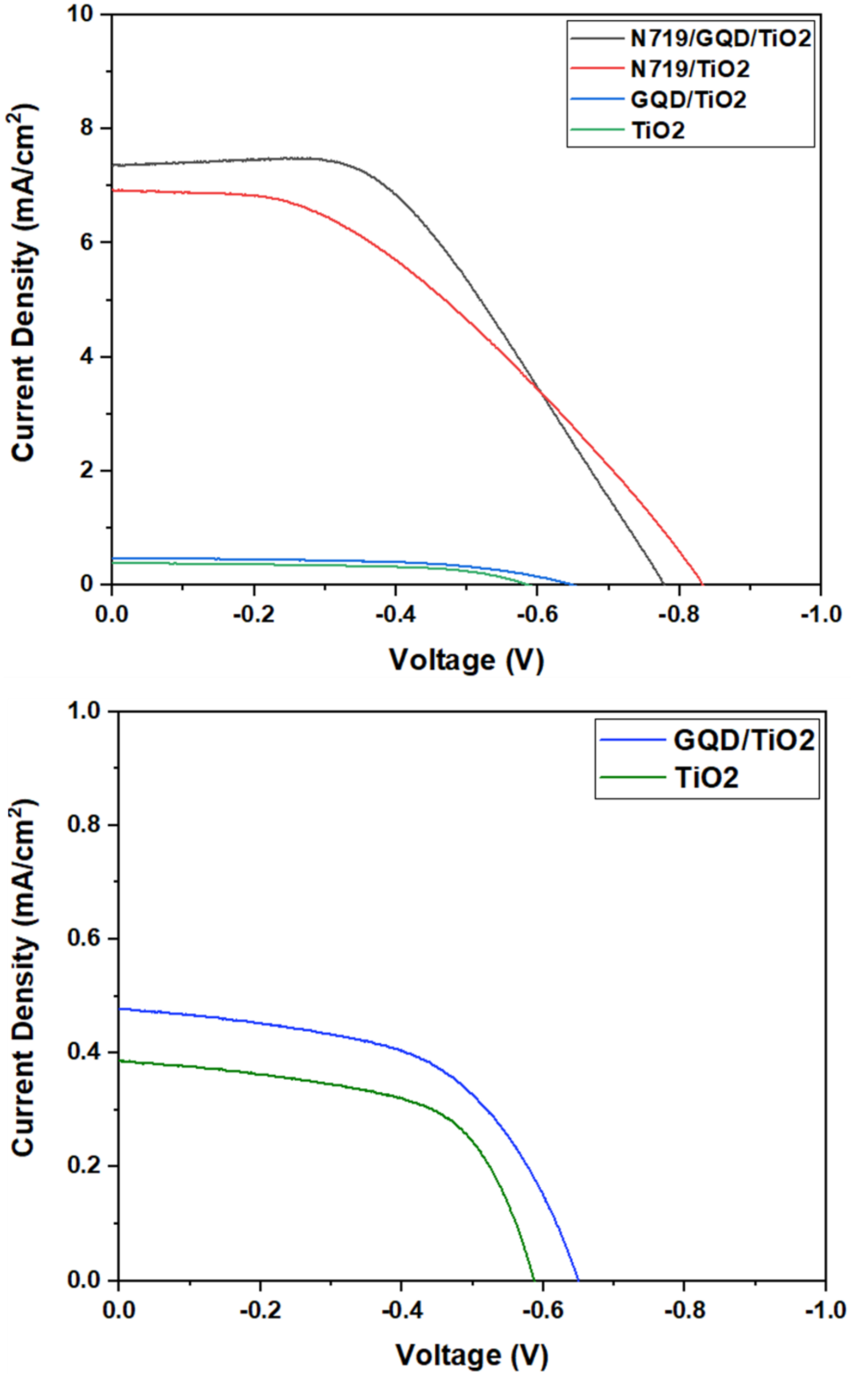

Figure 4.6 J-V characteristics curves of TiO_2, GQDs/TiO_2, N719/TiO_2, and N719/GQDs/TiO_2

Table 4.1 Summary of device parameters in solar battery using TiO_2, GQDs/TiO_2, N719/TiO_2, N719/GQDs/TiO_2

	Efficiency (%)	J_{sc} (mA/cm^2)	V_{oc} (V)	Fill Factor
TiO_2	0.133	0.386	0.586	0.590
GQDs/TiO_2	0.169	0.478	0.648	0.546
N719/TiO_2	2.346	6.928	0.832	0.407
N719/GQDs/TiO_2	2.784	7.344	0.778	0.487

electrode. The use of N719 dye result in the improved conversion efficiency and photocurrent intensity. The simultaneously use of GQDs and N719 can make the synergy effect of overall performance of the solar battery.

As shown in Figure 4.7, all of the TiO_2, GQDs/TiO_2, N719/TiO_2, N719/GQDs/TiO_2 show highly stable photocurrents under illumination for every 60 seconds. The N719/GQDs/TiO_2 electrode has a highest photocurrent density compared to that of the other three electrodes. The current densities of TiO_2, GQDs/TiO_2, N719/TiO_2, N719/GQDs/TiO_2 are 0.45, 0.57, 7.22, and 8.37 mA/cm^2, respectively. With the use of GQDs, the current densities of TiO_2 and N719/TiO_2 electrodes are increased by 26% and 16%, respectively. In addition, the use of GQDs and N719 dye in the TiO_2 electrode can improve the photovoltaic performance of the solar battery.

Electrochemical impedance spectroscopy (EIS) was used to evaluate the effects of co-sensitizers on the interfacial resistance of the photoanodes. EIS measurements were performed at a frequency range of 0.1Hz to 1MHz with an AC amplitude of 10 mV under AM1.5G illumination. The Nyquist plots of the photoanodes at their open-circuit potential are shown in Figure 4.8. The first semicircle in the high frequency indicates the resistance between Pt counter electrode and electrolyte, and the second semicircle in the low frequency represents the electron transfer interface between photoanode and electrolyte (R_{ct}).[10] At high frequency, the diameter of first semicircles is nearly comparable, indicating almost no charge transfer effect between Pt counter and electrolyte. The diameter of second semicircle of N719/GQDs/TiO_2 electrode at low frequency is significantly reduced compared to the that of TiO_2. It means that the use of

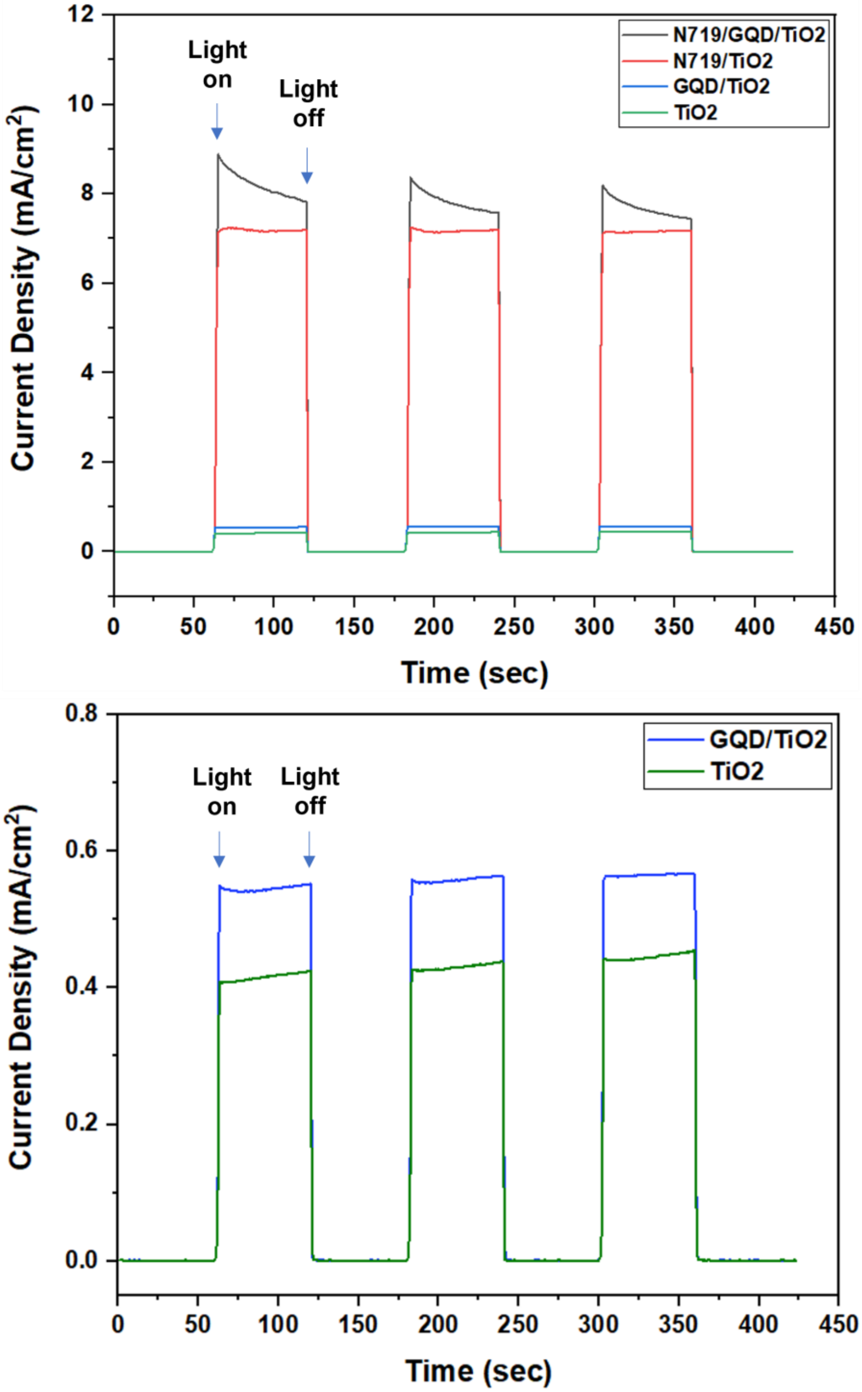

Figure 4.7 Chronoamperometry for the TiO_2, GQDs/TiO_2, N719/TiO_2, and N719/GQDs/TiO_2 illumination with light on and off in for every 60 seconds

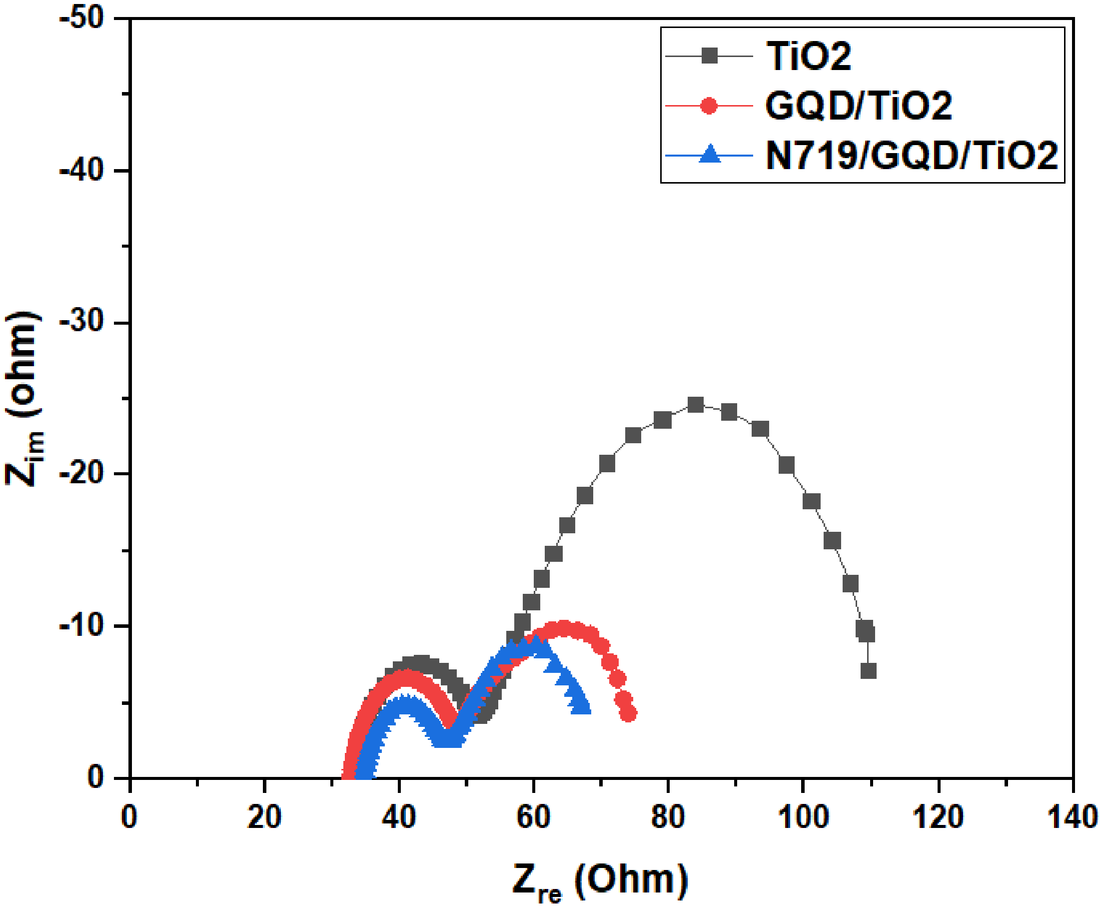

Figure 4.8 Nyquist plots of the photoanodes under illumination

GQDs and N719 is highly effective to reduce the interfacial resistance between photoanode and electrolyte. Thus, GQDs plays key role in transferring electrons and holes, resulting in the higher power conversion efficiency (PCE).

In Figure 4.9, the charge/discharge test was carried out in the dark and under illumination, ranging from 2V to 1.2V with 0.1C-rate. The discharge capacity of N719/GQDs/TiO2 is increased by 11.3% and 26% compared to the TiO_2 under illumination and in the dark, respectively. The capacity fading was found only in samples under illumination.

4.6 Conclusion

GQDs and N719 dye are used as co-sensitizer to improve light absorption. Their synergy effects were examined by electrochemical analysis, and the existence of GQDs and N719 was confirmed by XRD, Raman, FT-IR. The portion of GQDs in the GQDs/TiO2 can be estimated by EDX analysis. The use of both GQDs and N719 dye can help to improve the energy conversion efficiency and discharging capacity under illumination and reduce the interfacial resistance between the photoanode and electrolyte.

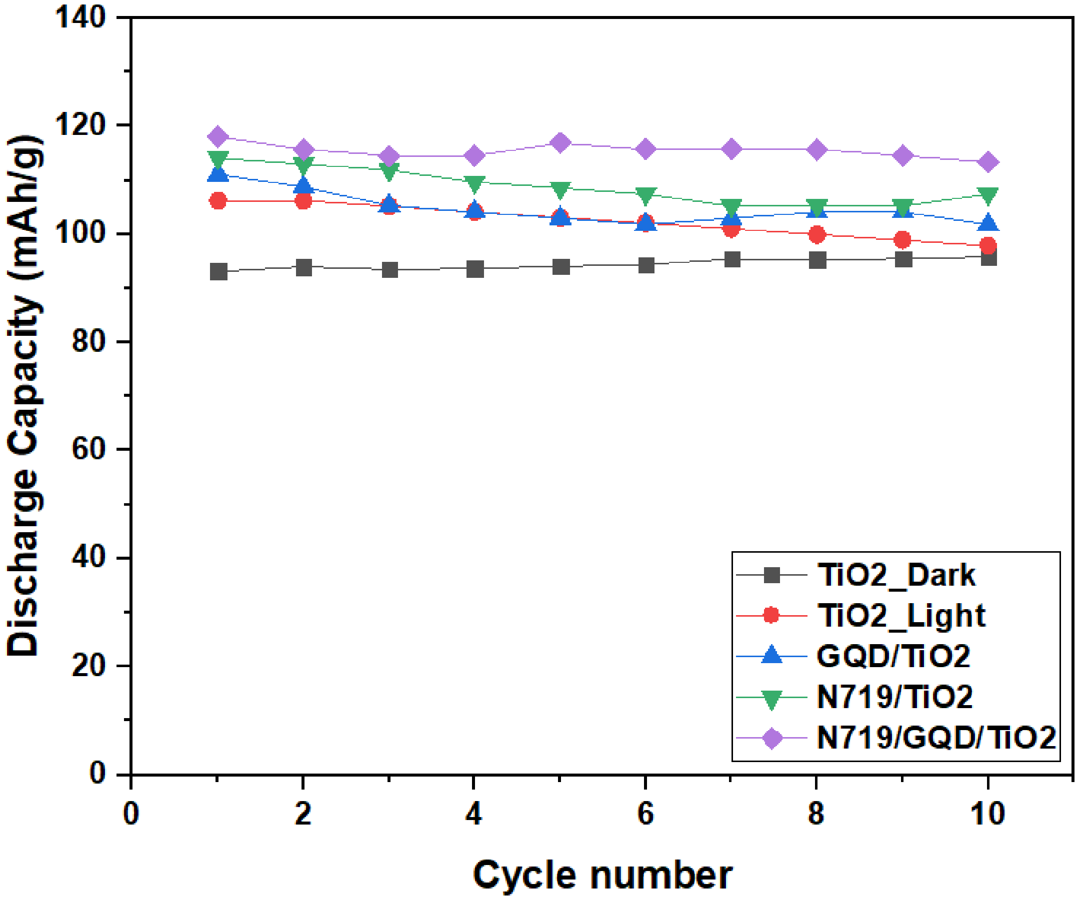

Figure 4.9 Discharge capacity vs. cycle number graph of the photoanodes

Reference

1. Qian, R.; Zong, H.; Schneider, J.; Zhou, G.; Zhao, T.; Li, Y.; Yang, J.; Bahnemann, D. W.; Pan, J. H. J. C. T., Charge carrier trapping, recombination and transfer during TiO2 photocatalysis: An overview. **2019,** *335*, 78-90.

2. Sachs, M.; Pastor, E.; Kafizas, A.; Durrant, J. R. J. T. j. o. p. c. l., Evaluation of surface state mediated charge recombination in anatase and rutile TiO2. **2016,** *7* (19), 3742-3746.

3. Yu, Z.; Liu, H.; Zhu, M.; Li, Y.; Li, W. J. S., Interfacial charge transport in 1D TiO2 based photoelectrodes for photoelectrochemical water splitting. **2021,** *17* (9), 1903378.

4. Sharif, N. F. M.; Kadir, M.; Shafie, S.; Rashid, S. A.; Hasan, W. W.; Shaban, S. J. R. i. P., Charge transport and electron recombination suppression in dye-sensitized solar cells using graphene quantum dots. **2019,** *13*, 102171.

5. Low, F. W.; Lai, C. W. J. R.; Reviews, S. E., Recent developments of graphene-TiO2 composite nanomaterials as efficient photoelectrodes in dye-sensitized solar cells: A review. **2018,** *82*, 103-125.

6. Muhammad, N.; Mohtar, M.; Ramli, M.; Shafie, S.; Shaban, S.; Yusof, Y. J. I. J. o. M., Mechanics; Manufacturing, Enhancement of Dye Sensitized Solar Cell by Adsorption of Graphene Quantum Dots. **2020,** *8* (3).

7. Bokare, A.; Chinnusamy, S.; Erogbogbo, F. J. C., TiO2–graphene quantum dots nanocomposites for photocatalysis in energy and biomedical applications. **2021,** *11* (3), 319.

8. Hao, X.; Jin, Z.; Xu, J.; Min, S.; Lu, G. J. S.; Microstructures, Functionalization of TiO2 with graphene quantum dots for efficient photocatalytic hydrogen evolution. **2016,** *94*, 237-244.

9. Gupta, B. K.; Kedawat, G.; Agrawal, Y.; Kumar, P.; Dwivedi, J.; Dhawan, S. J. R. A., A novel strategy to enhance ultraviolet light driven photocatalysis from graphene quantum dots infilled TiO 2 nanotube arrays. **2015,** *5* (14), 10623-10631.

10. Hsu, C.-P.; Lee, K.-M.; Huang, J. T.-W.; Lin, C.-Y.; Lee, C.-H.; Wang, L.-P.; Tsai, S.-Y.; Ho, K.-C. J. E. A., EIS analysis on low temperature fabrication of TiO2 porous films for dye-sensitized solar cells. **2008,** *53* (25), 7514-7522.

Chapter 5. Conclusions

The unique photo-rechargeable battery was invented by integrating photovoltaic and energy storage systems in one device. The critical incentives for physically direct integration are the reduction of the number of materials, high volumetric and gravimetric energy density, minimization of energy losses. Lithium iron phosphate (LFP) and titanium dioxide (TiO_2) paste were used as the working and counter electrodes, respectively. The characteristics of the photo-rechargeable battery were investigated by electrochemical measurements, such as LSV, CV, chronoamperometry, and charging and discharging test. The photovoltaic efficiency of the battery was calculated based on the LSV curves in the dark and under illumination. The energy conversion efficiency of the battery under illumination has higher than the battery in the dark. The photocurrent densities of the battery in the dark and under illumination were measured every 60 seconds. From the chronoamperometry curve, the stability of the photo-chargeable battery was evaluated. The anodic and cathodic peaks are observed, and the cut-off voltage is determined by CV. The specific discharging capacity under illumination is 9.6% higher than that of the battery under dark.

Among the carbon-based materials available, graphene quantum dots (GQDs), a new type of carbon-based material, are currently under the spotlight and also have been widely applied in photocatalysis, energy storage and conversion, biochemistry, and immunology applications due to their high surface area, low toxicity, and broad optical absorption. In general, the synthesis methods of nanomaterials can be classified by the bottom-up approach and the top-down approach. In this work, GQDs were successfully synthesized by the electrochemical exfoliation method, one of the top-down approaches. Graphite was employed as a starting material and was heated at high temperatures to make more defects before the electrochemical exfoliation. The characteristics and properties of GQDs were investigated by XRD, FT-IR, Raman, TEM, UV-vis, and PL. The synthesized GQDs has a crystalline structure and a variety of oxygen-containing functional group at the surface and the edge. The increase in the intensity of D/G bands indicates that many defects were made during the synthesis, and the morphology and size distribution of GQDs were examined. In addition, the absorption, emission, and excitation peaks were measured to identify their optical properties.

To improve the photovoltaic performance of the battery, the co-sensitizers (GQDs and N719 dye) were used, and their effects were investigated by LSV, chronoamperometry, EIS, and charging and discharging test. In order to confirm the presence of GQDs and N719 in the TiO_2, GQDs/TiO_2, N719/TiO_2, N719/GQDs/TiO_2 electrodes, the XRD, Raman, FT-IR, and EDX characterizations were used. The overall portion of GQDs in the GQDs/TiO_2 electrode can be estimated at around 2.7 wt%. The GQDs act as a bridge between TiO_2 and N719, affecting the absorption range. The conversion efficiency of N719/GQDs/TiO_2 under illumination reaches 2.784 % and is 21 times higher than TiO_2. In addition, the photocurrent of N719/GQDs/TiO_2 has 19 times higher than TiO_2. The interfacial resistance of the N719/GQDs/TiO_2 electrode is significantly decreased than that of the pristine TiO_2 electrode. Due to the effect of conversion efficiency and interfacial resistance, the discharging capacity of N719/GQDs/TiO_2 is significantly increased compared to the TiO_2.